Università degli studi di Padova

School of Science

Department of Chemical Sciences

Master Degree in Materials Science

Understanding and resolving optoelectronic losses for highly efficient perovskite/silicon tandem solar modules

Supervisor: Submitted by:

Prof. Moreno Meneghetti   Francesco Toniolo

Co-Supervisor:

Prof. Stefaan De Wolf

Opponent supervisor

Prof. Chiara Maccato

Academic year 2021/2022

Abstract

Among renewable technologies, photovoltaics has become the cheapest form of energy production. So far, the wider portion of the solar panel market is led by crystalline silicon (c-Si) because of its efficiency, reliability, and affordable manufacturing. Owing to their high efficiency, low-cost solution-processability, and tunable bandgap, hybrid organic-inorganic perovskite solar cells (PSCs) are a new promising class of semiconducting materials for the next generation of solar panels. Moreover, these perovskites perfectly couple as top-cell candidates for integration with c-Si bottom-cells in tandem configuration to overcome the intrinsic efficiency limit of Shockley-Queisser (S-Q). Nowadays, a huge research effort has allowed to achieve perovskite performances comparable with the best c-Si solar cell. Most of the research is focused on the improvement at the device level with the adoption of new materials and the development of new deposition techniques. However, despite its importance, few studies have investigated the transition from cell to module level and the operation of the perovskites under real-world conditions. A limiting factor in this translation was the lack of stable performances and fast degradation of the perovskite. Therefore, investigating encapsulation and packaging strategies to increase the lifetime of perovskite-based photovoltaics is of paramount importance. In this work, we investigate the encapsulation of perovskite/silicon tandem solar cells and the fabrication of minimodules that have been tested in lab experiments and outdoor conditions. For the first time, we recreated an experimental setup that allows us to mimic the different angles of incidence of the incoming light, understanding the behavior of different module architectures and studying the performances under a real world environment. Part of the results of this thesis have been published in Monolithic Perovskite/Silicon Tandem Photovoltaics with Minimized Cell-to-Module Losses by Refractive-Index Engineering (ACS Energy Letter, 2022, 7, 2370-2372); Efficient and Reliable Encapsulation of Perovskite/Silicon Modules with Thermoplastic Polymers (in preparation); Angular-Dependent Performances of Perovskite/Silicon Tandem in Experimental and Outdoor Conditions (in preparation).

Contents

Chapter 1

Introduction

The importance of solar energy

One of the biggest challenges that human society is facing in the 21st century is the continuously rising in the world's energy demand. Some studies[1–3] predict a world population of 9 billion around 2040, in contrast to the 7 billion people living on the planet in 2014. Since 2009, the total global primary energy consumption has continued to increase with a rate of 15.10% in 10 years. Nowadays, fossil fuels dominate the energy production sector. However, their consumption is much faster than their generation, therefore are considered non-renewable sources and are not sustainable towards the future predictions. Moreover, the increased consumption of fossil fuels complicates the extraction of gas and oil (the primary fossil fuels) rising their price and environmental impact. To this, we add that energy, steel, and concrete production (primary industry sectors) generate the largest amount of CO_2 emitted into the atmosphere contributing to the effects of climate change.

In order to keep the global temperature rising below 1.5°C, new renewable energy production technologies are required. Contrary to fossil fuels, these forms of energy are regenerated over a short time span and ideally illimited. The most important renewables are solar, wind, hydroelectrical, geothermal, and recently, nuclear. Of course, to overcome the climate challenge, these technologies by themselves are not able to satisfy the world's energy demand, but they will if combined with storage systems and a suitable distribution network. The work of this thesis will focus on solar energy and photovoltaics, the process of converting sunlight into electricity, using innovative and powerful technologies.

To understand the potential of solar energy we can consider a land size of around 8400 km^2, covered with currently available state-of-the-art commercial photovoltaics (PV) technology, the annual energy yield would be at least similar if not exceed the energy yield from the annual oil production of the same field, ~950-1000 TWh.[4] Moreover, PV has also become the cheapest form of energy production.[5] In the last decade over 100MW of new photovoltaic installations have been added every day, leading to a global installed capacity of around 655GW (figure 1.1), which is expected to grow up to 4500GW by 2050.[6] Indeed, this expected exponential rise is the driving factor that constantly pushes researchers and

industries to improve the actual technology. Industrially PV manufacturing is mostly based on crystalline Silicon (c-Si) which has significantly progressed in the past 10 years moving from ≈15% to more than 21% thanks to improvements in the cell level and module design which will be further discussed later in this work.

However, PV technologies, to be competitive with standard energy production need to further grow with the improvements of the actual state of the art and the introduction of new light-harvesting materials. Between these new materials, halide perovskite is attracting the scientific community's attention because of its structural and optoelectronic properties that make it a promising candidate as solar material. Indeed, halide perovskites have semiconducting properties close to an ideal photo-absorbing material. These properties can be summarized with *i* a steep absorption coefficient, allowing for a cheap thin-film technology; *ii* high defect tolerance, which reduces unwanted photo-carriers losses enabling high voltage output; *iii* a tunable bandgap, allowing for the implementation of multijunction configurations, achieving record power conversion efficiencies (PCE). However, the lack of stability of these properties is currently hindering the early commercialization of the perovskite technology. Indeed, the degradation and the behavior of this material under real-world conditions still need to be deeply studied. In this work, the optical losses, and the real-world behavior of Perovskite/Silicon tandem solar cells will be analyzed and discussed.
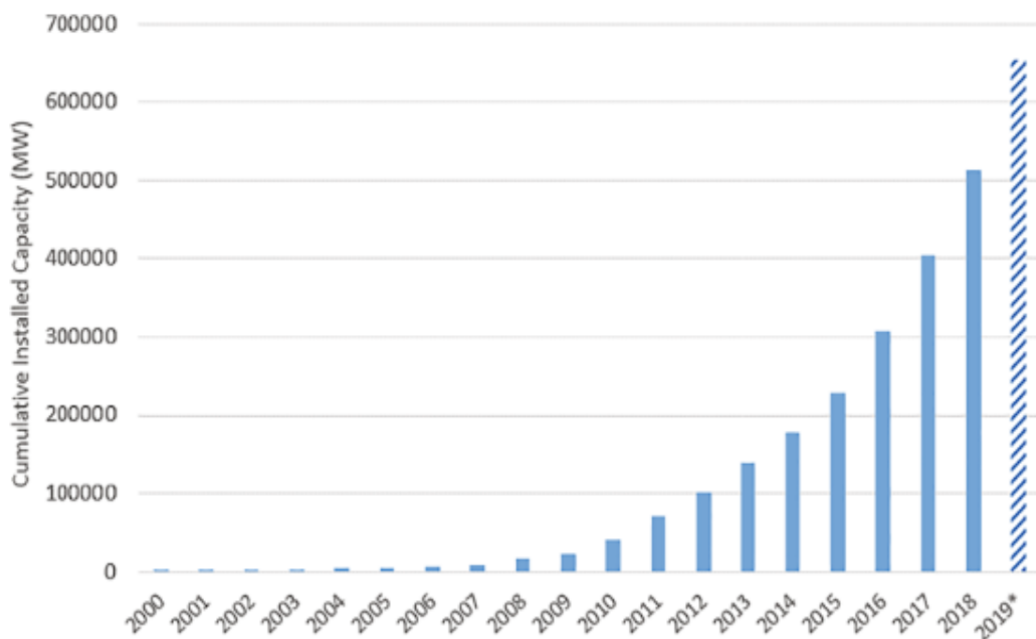

Figure 1.1: Global trend of installed capacity addition of PV energy.

Semiconductor Physics

Solar cells working principle is based on a class of material called semiconductors which can be defined as insulators with a sufficiently small energy gap to allow the promotion of electrons from the valence to the conduction band, just supplying a proper amount of energy. Indeed, unlike metals, in semiconductors, the resistivity decreases with temperature thanks to the promotion of electrons to the conduction band (CB). In metals instead, the number of charge carriers is constant with temperature, but their mobility decreases.[7] When a very large number of atoms come together each atomic orbital spilt into a very large number of levels, so close together in energy that they effectively form a continuum, called band of allowed levels. The energy distribution of the bands depends on the electronic properties of the atoms and the strength of the bonding between them. The highest occupied band, which contains the valence electrons is called the valence band (VB), while the lowest unoccupied band is called the conduction band (CB). The Fermi level (E_f) determines the energetic of the system and usually lies in between the CB and VB. The interval of prohibited values of energy for an electron is called the energy gap (or band gap E_g) and it can be also seen as the difference in energy between the conduction and the valence band. Once the semiconductor crystal structure is known, the band diagram can be predicted exactly. The adopted crystal structure will depend on the number of valence electrons of the atom and on the minimization energy principle. In general, in crystalline structures where all the valence electrons are used in bonding, a band gap arises. When an electron is promoted from the VB to the CB a lack of negative charge (thus a positive charge) is formed and is defined as a hole in the VB, which can be characterized in the same way as conduction electrons.[8,9]
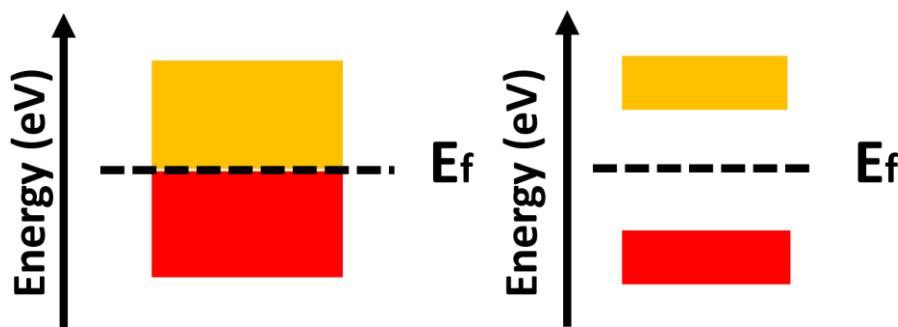

Figure 1.2: Schematic representation of the valence and conduction bands for a metal (left) and for a semiconductor (right) in which the two bands are separated by an interval of forbidden energies called energy gap.

So far, only intrinsic semiconductors have been described, thus, as mentioned before, the only energy levels permitted are the levels that arise from the overlap of the atomic orbitals. The properties of those bands determine the position of the Fermi level, called intrinsic Fermi level, (E_{Fi}), and the density of carriers that have enough thermal energy to cross the band gap and conduct electricity. For an intrinsic semiconductor, at room temperature, the conductivity is generally very small. Introducing foreign atoms in the semiconductor crystal structure allows modification of the carrier concentration in the material by introducing a perturbation of the local distribution of electronic energy levels. This strategy is called "doping" and can be executed with several approaches. However, the most common is the substitution of a lattice atom with one that belongs to a different group of the periodic table, and depending on the number of valence electrons that presents the new atom, the density of majority charge carriers will change. Figure 1.3 shows the substitution of a silicon atom with Boron or Phosphorus. When introducing a phosphorus atom into the c-Si lattice, four of the five phosphorus atom's valence electrons will form bonds with the four neighboring Si atoms. The fifth valence electron cannot take part in forming a bond and it will weakly interact with the phosphorus atom. With the absorption of thermal energy (at room temperature), it can be easily liberated from the phosphorus atom, and once free, the electron can move throughout the lattice. This kind of impurity atoms increases the electron density in the crystal leading to the so-called n-type doping. Atoms that present an excess of electrons are called "donors" (figure 1.3a). Conversely, an atom defined as "acceptor" such as Boron in the Silicon crystal lattice, presents a missing electron or an extra positive hole (figure 1.3b). The acceptor becomes ionized by removing a valence electron from another bond to complete the bonding between it and its four neighbors. The injection of holes given by acceptors impurities is called p-type doping. A new Coulomb interaction arises between the newly introduced charge and the nearby atom, leading to a perturbation of the periodic crystal potential. Therefore, inserting donor and acceptor atoms into the lattice modifies the energy levels by allowing new ones inside the forbidden bandgap. For example, the excess electron given by the phosphorus impurity will generate an energy level close to the CB edge with energy E_D. Similarly, the acceptor will generate a new energy level E_A close to the VB edge (figure 1.4). Doping also influences the position of the Fermi energy. According to equations 1.1 and 1.2, when we increase the electron concentration by increasing the donor concentration the Fermi energy will increase, which is represented by bringing the Fermi energy closer to the CB in the band diagram. In the p-type material, the Fermi energy is moved closer to the VB.

$$Ec - E_F = K_B T \, ln\left(\frac{N_C}{N_D}\right) \tag{1.1}$$

$$E_F - E_V = K_B T \, ln\left(\frac{N_V}{N_A}\right) \qquad (1.2)$$

Where Nc and Nv are the effective densities of states of the conduction and valence bands respectively, and N_D and N_A denote the density of the ionized donor and acceptor atoms, respectively.

Before getting into the details about the solar cells working principle, it is mandatory to define what is a p-n junction and its properties. Indeed, this junction is the classical model of a solar cell. Let us consider two different semiconductors isolated, one n-type and the second p-type. While the semiconductors are isolated the charge neutrality is granted but when the two are brought together, a very large difference in electron concentration between n- and p-type regions causes a diffusion current of electrons from the n-type material across the junction into the p-type material. Similarly, the difference in hole concentration causes a diffusion current of holes from the p- to the n-type material. When the electrons and holes move to the other side of the junction, they leave behind fixed exposed charges (the ionized lattice atoms). An electric field forms between the positive ion cores in the n-type material and negative ion cores in the p-type material. Hence, the electric field quickly sweeps free carriers out, leading to a depletion of free charge carriers. A "built-in" potential V_{bi} is formed at the junction due to the electric field. The diffusion currents continue to flow until the forces acting on the charge carriers compensate each other. Once the junction reaches the equilibrium, we can recognize three different regions, the two homogeneous p or n regions, far from the junction, and the so-called "depletion region" obtained from the built-in potential.

If an external bias (V_a) is applied to the junction, two different cases can be distinguished. Under equilibrium conditions, we define the build-in potential as negative in the p-type region with respect to the n-type ones. If we apply a negative external bias with respect to the potential of the p-type region, the potential difference across the p-n junction will
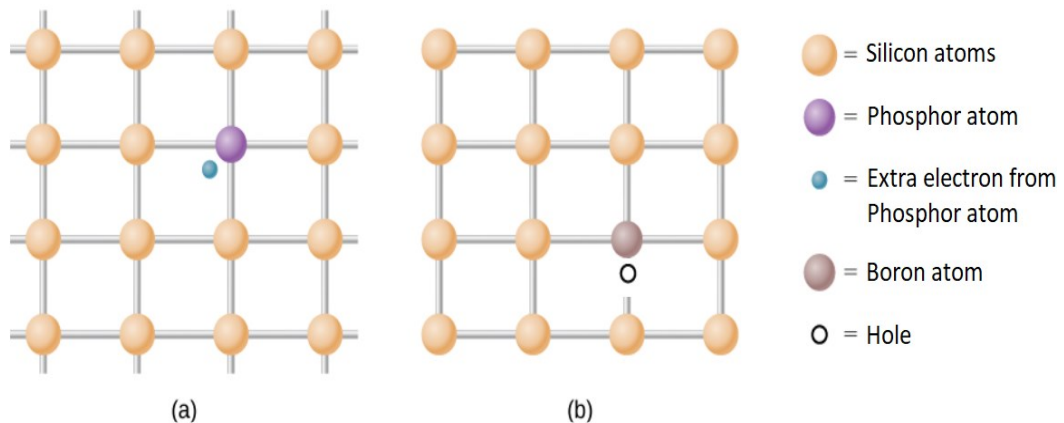

Figure 1.3: Introduction of donor (a) and acceptors (b) impurities into the Silicon lattice.
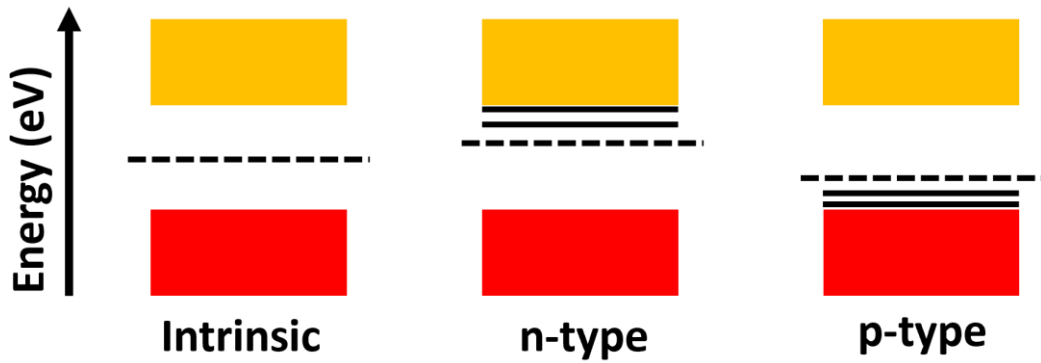
Figure 1.4: Energy levels schematic of undoped (left) and doped (right) semiconductors.

increase, generating a wider depletion region. This condition is referred to as the "reverse-bias" condition (figure 1.5a). On the contrary, the "forward-bias" voltage is applied when the external voltage is positive with respect to the potential of the p-type region. Under this condition, the build-in potential will be weakened (figure 1.5b), ending up in the narrowing of the depletion region and an accumulation of minority carriers (electrons in the p-type region and holes in the n-type one) at its edge. As result, a minority carriers injection occurs. This diffusion causes the so-called recombination current density, J_{rec} since the diffusing minority carriers recombine with the majority carriers in the bulk. When no voltage is applied this current is completely compensated by thermal generation current, J_{gen}, which is caused by the drift of minority carriers. With a certain bias, the external net current is described by equation 1.3, in which J_0 is the saturation current density (also known as dark current density) that depends on the fundamental semiconductor parameters.

$$J(V_a) = J_{rec}(V_a) - J_{gen}(V_a) = J_0\left[exp\left(\frac{qV_a}{K_BT}\right) - 1\right] \quad (1.3)$$
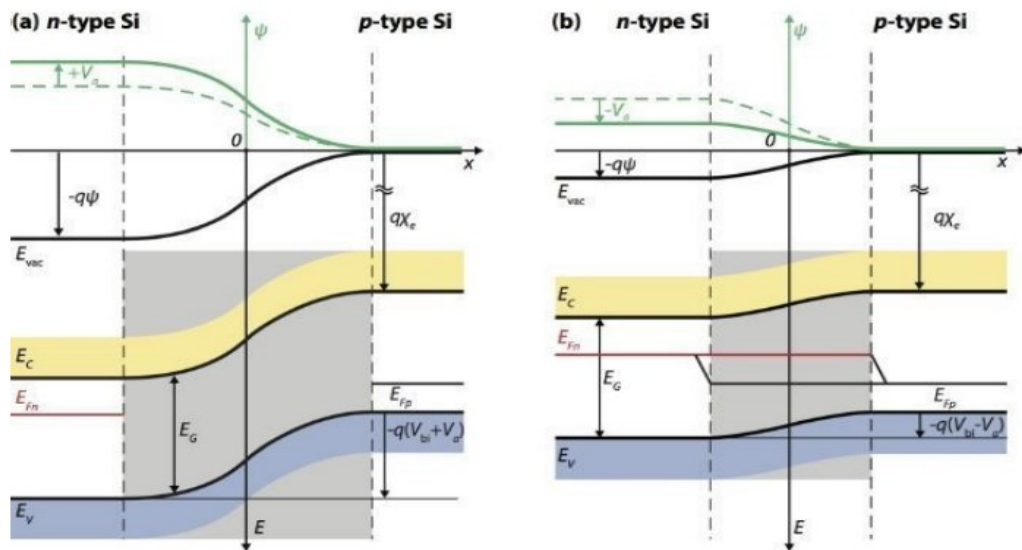

Figure 1.5: Energy band diagram and electrostatic potential (green) of a p-n junction under reverse bias (a) and forward bias (b) conditions.

Under illumination, light creates additional electron-hole pairs in the semiconductor, therefore the minority carrier's concentration deeply increases leading to a strong injection of holes and electrons towards the p-type and n-type region respectively. The flow of the photogenerated carriers causes the so-called photogeneration current density, J_{ph}, which adds to the thermal-generation current, J_{gen}.

Solar cells Fundamentals

A solar cell is an electronic device that directly converts sunlight into electricity. When light strikes the solar cell, current and voltage are generated. The working principle of solar cells is based on the photovoltaic effect, i.e., the generation of a potential difference at the junction of two different materials in response to electromagnetic radiation. Different steps characterize this process. Firstly, in an ideal semiconductor, the absorption of a photon with energy $E_{ph} = h\nu$ (where h is the Planck constant and ν is the photon frequency) greater than the material's energy gap, allows the promotion of an electron to an excited state with the consequential creation of an electron-hole pair. Photons with energy $E_{ph} < E_g$ will traverse the material without any interaction. Under standard conditions, the electron-hole pair will recombine, i.e., the electron will fall back to the initial energy level. The energy will then be released either as a photon (radiative recombination) or transferred to other electrons or holes or lattice vibrations (non-radiative recombination). In order to block this recombination and collect the energy stored in the electron-hole pair for performing work in an external circuit, extraction layers (one extraction layer per each type of carrier) are required on both sides of the absorber, such that electrons and holes can flow and generate a charge current. For example, the simplest extraction layer is an n- or p-type material, based on the type of charge carrier that needs to be extracted. A solar cell has to be designed such that the electrons and holes can reach the extraction layers before they recombine, i.e. the time it requires the charge carriers to reach these layers must be shorter than their lifetime. This requirement limits the thickness of the absorber. Finally, the charge carriers are extracted from the solar cells with electrical contacts so that they can perform work in an external circuit. The energy of the electron-hole pairs is finally converted to electric energy. After the electrons have passed through the circuit, they will recombine with holes at a metal-absorber interface. Limiting the recombination of carriers is fundamental to guarantee a proper current and voltage generation and there are semiconductors more suitable as solar material than others. Indeed, semiconductors may have direct or indirect bandgap. In direct bandgap, the minima and the maxima of the CB and VB coincide, while

in indirect bandgaps are shifted in the k-space. Figure 1.6 shows the energy-momentum space of the electrons. On the vertical axis, the energy state in the electronic bands is plotted. On the horizontal axis, the momentum of the charge carrier is shown. This momentum is also called the crystal momentum and is related to the wave vector k of the electron. For a direct band gap material, the highest point of the valence band is vertically aligned with the lowest point of the conduction band (figure 1.6a). This means that exciting an electron from the valence to the conduction band requires only the energy provided by
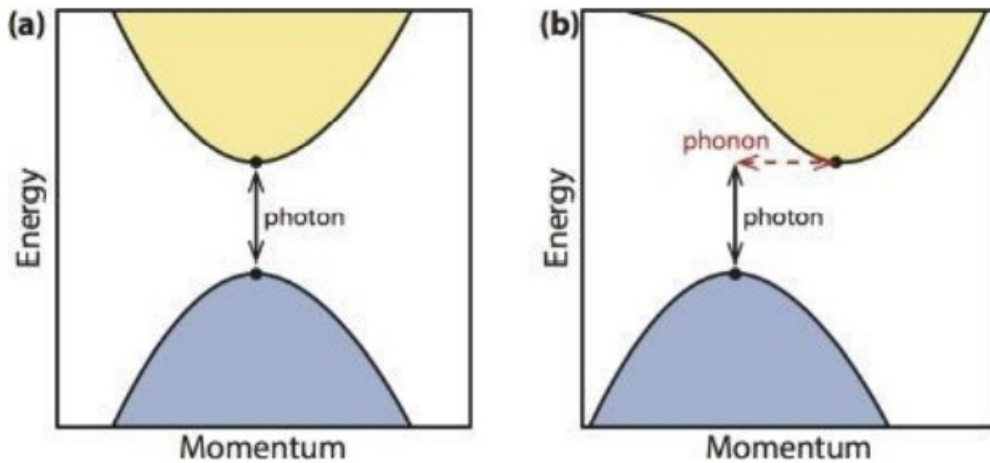

Figure 1.6: Illustration of the energy-momentum space for a semiconductor with a) direct and b) indirect band gap.

a photon without any additional momentum transfer. In contrast, for an indirect band gap, the highest point of the valence band is not aligned with the lowest point of the conduction band, as shown in (Figure 1.6b). Therefore, since the momentum needs to be conserved exciting an electron from the valence to the conduction band requires energy provided by a photon and the momentum will be conserved thanks to a phonon. The lattice vibrations can also be described as waves and as particles, called phonons. A phonon, therefore, is a quantized mode of lattice vibrations. It is clear that the excitation of an electron-induced by photon absorption is more likely to happen for direct band gap materials than for indirect band gap materials and hence the absorption coefficient for direct band gap materials is significantly higher than for indirect band gap materials. The same principle makes the reverse process of radiative recombination more probale in a direct band gap material. In an indirect band gap material, additional momentum is required to make the electron and hole recombine, and being crystalline silicon an indirect band gap material, the radiative recombination is less efficient.

Solar cells characterization

As previously mentioned, only photons with appropriate energy can be absorbed generating electron-hole pairs in a semiconductor material. Therefore, it is important to know the spectral distribution of the solar radiation, i.e. the number of photons of particular energy as a function of the wavelength λ. Two quantities are used to describe the solar radiation spectrum, namely the spectral irradiance $I_{e\lambda}$, which refers to the radiation that is received by the ground, and the spectral photon flux Φ_{ph} (λ), defined as the photon flow per unit area. With a surface temperature of around 6000K, the Sun is considered a perfect black body that emits a spectrum as the one shown in figure 1.7 (black line). The spectrum outside the atmosphere of Earth is already significantly different. It is called the AM0 spectrum because no (or "zero") atmosphere is traversed. Obviously, the solar spectrum reaching the solar cell differs from the AM0. When the solar radiation passes through the atmosphere of Earth, there is an attenuation due to scattering and absorption given by air molecules. The distance that the sunlight has to travel through the atmosphere is the most important parameter, and determines the solar irradiance under clear-sky conditions. This distance is the shortest when the Sun is at the zenith, i.e. directly overhead. The ratio of an actual path length of the sunlight to this minimal distance is known as the optical air mass. When the Sun is at its zenith the optical air mass is unity and the spectrum is called the air mass 1 (AM1) spectrum. When the Sun is at an angle θ with the zenith, the air mass is given by

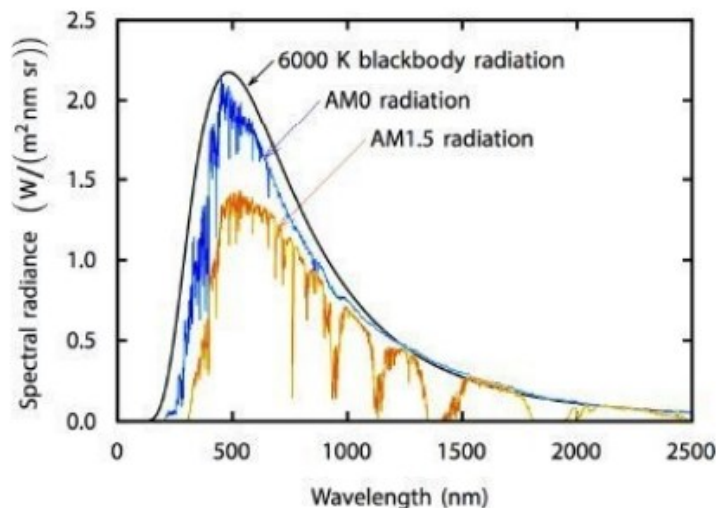$$AM = \frac{1}{\cos \theta} \tag{1.4}$$

Figure 1.7*: Different solar spectra: the blackbody spectrum of a blackbody at 6000K, the extraterrestrial AM0 spectrum, and the AM1.5 spectrum.*

Since solar cells and photovoltaic modules are installed in different worldwide locations it is therefore important to define unambiguous conditions that allow a comparison of all different solar cells and PV modules. These conditions are the standard test conditions (STC), characterized by an irradiance of 1,000 Wm^{-2}, an AM1.5 spectrum, and a cell temperature of 25° C. The AM1.5 spectrum is a reference solar spectral distribution, being defined in the International Standard IEC 60904-3. This spectrum is based on the solar irradiance received on a Sun-facing plane surface tilted at 37° to the horizontal.

The key performance parameters to determine the efficiency of a solar cell are the short circuit current density (Jsc), the open circuit voltage (Voc), the Fill Factor (FF), and maximum power point (P_{MAX}). These parameters are determined from the illuminated J-V characteristic curve, which combined with the dark J-V provides all the required information for the basic characterization of solar cells. The short circuit current Isc is the current that flows through the external circuit when the electrodes of the solar cell are short circuited i.e. when the voltage across the solar cell is zero. The short circuit current of a solar cell depends on many factors such as the photon flux incident on the solar cell, the area of the solar cell, reflection losses or parasitic absorption, the thickness of the photo-absorber, the absorption coefficient of the photo-absorber, and many more. In order to remove the dependence of the solar cell area from Isc, the short-circuit current density (Jsc) is often used to describe the maximum current delivered by a solar cell. In the ideal case, Jsc is equal to the photogenerated current density (J_{ph}) that is defined by the equation 1.5,

$$J_{ph} = qG \left(L_n + W + L_p \right) \tag{1.5}$$

in which G is the generation rate, W is the depletion region width and L_n and L_p are the minority carriers' diffusion lengths of electrons and holes respectively. From this expression, we can derive that, only carriers generated in the depletion region and in the regions up to the minority-carrier diffusion length from the depletion region can contribute to the photogenerated current. When designing a solar cell, the thickness of the absorber should not be greater than the region from which the carriers contribute to the photogenerated current. In turn, this will minimize the unwanted recombination mechanisms (see next paragraph)

The open-circuit voltage (V_{OC}) is the maximum voltage available from a solar cell, and this occurs at zero current. It corresponds to the forward bias voltage, at which the dark current density compensates the photocurrent density and, assuming that the net current is zero, it can be calculated from the equation 1.5.

$$J(V_a) = J_{rec}(V_a) - J_{gen}(V_a) - J_{ph} = J_0 \left[exp\left(\frac{qV_a}{k_BT}\right) - 1 \right] - J_{ph} \tag{1.6}$$

Thus, the expression for the Voc is:

$$V_{OC} = \frac{k_B T}{q} ln\left(\frac{J_{ph}}{J_0} + 1\right) \approx \frac{k_B T}{q} ln\left(\frac{J_{ph}}{J_0}\right) \quad (1.7)$$

Where the final expression is obtained considering $J_{ph} \gg J_0$. The latter (J_0, also called recombination current) depends on the recombination effects inside the solar cell and is mostly linked to the diode performances of the solar cell in dark. Thus, the Voc is a measure of the amount of recombination events that occur in the device.

The short-circuit current and the open-circuit voltage are the maximum current and voltage respectively from a solar cell. However, at both of these operating points, the power generated by the solar cell is zero. The fill factor (FF) is a parameter that, in conjunction with Voc and Isc, determines the maximum power from a solar cell. The FF is defined as the ratio of the maximum power from the solar cell to the product of V_{oc} and I_{sc} so that:

$$FF = \frac{J_{mpp}V_{mpp}}{J_{sc}V_{oc}} \quad (1.8)$$

J_{MPP} and V_{MPP} denote the maximum power point (MPP) of the solar cell, therefore the point on the J-V characteristic curve at which the solar cell has the maximum power output (P_{max}).

The power conversion efficiency (η or PCE) is calculated as the ratio between the maximal generated power and incident power.

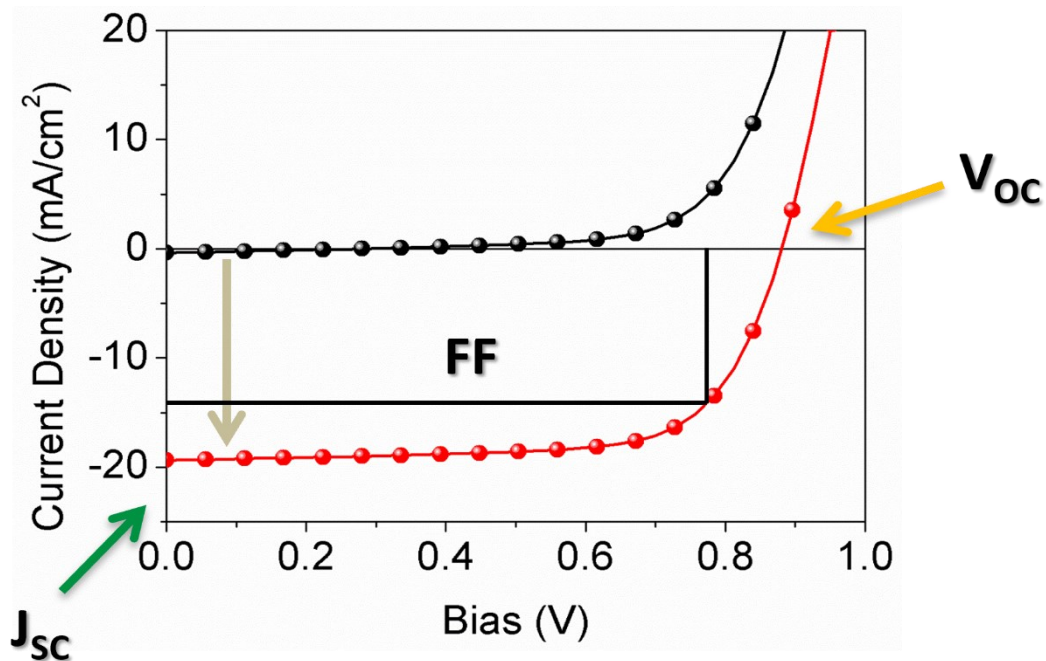$$\eta = \frac{P_{max}}{I_{in}} = \frac{J_{mpp}V_{mpp}}{I_{in}} = \frac{J_{sc}V_{oc}FF}{I_{in}} \quad (1.9)$$

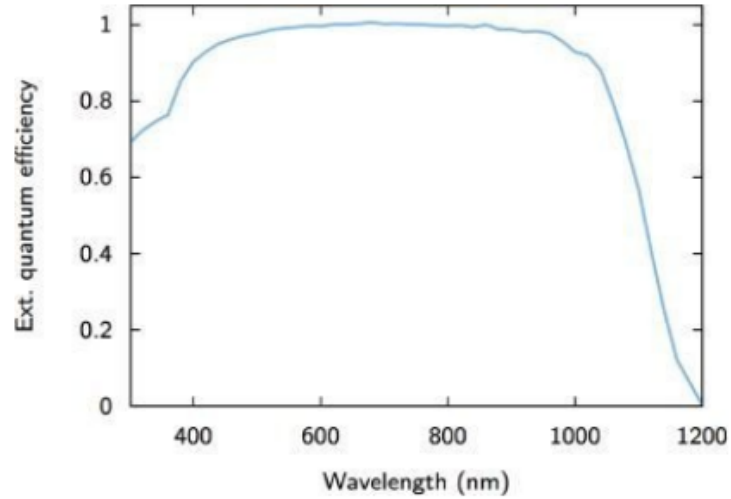*Figure 1.8: J-V characteristic curve of a solar cell in the dark (black) and under illumination (red).*

Figure 1.9: The external quantum efficiency of a high-quality crystalline silicon-based solar cell.

With I_{in} the incident power of light. For sunlight and standard testing protocols, I_{in} is considered 1000 W/m^2 of 100mW/cm^2. Therefore, a solar cell under the Sun at standard conditions, with a Voc of 1.8 V, a Jsc of 18mA/cm^2, and a FF of 75% has a PCE of 24.5%, equal to a power generation of 24.5 mW/cm^2.

With the J-V curve, many different aspects can be evaluated of our solar cells. To gain further insight into the performance of a solar cell and to better understand the losses mechanisms, another fundamental characterization is the external quantum efficiency (EQE(λ)). The EQE(λ), is the fraction of photons incident on the solar cell that create electron-hole pairs in the absorber which are successfully collected, and it is defined as follows

$$EQE(\lambda) = \frac{I_{ph}(\lambda)}{q\Psi_{ph,\lambda}} \qquad (1.10)$$

In which q is the elementary charge and $\Psi_{ph,\lambda}$ is the spectral photon flow incident on the solar cell and is usually determined by measuring the EQE signal of a calibrated photodiode under the same light source. The EQE is wavelength dependent and is usually measured by illuminating the solar cell with monochromatic light of wavelength λ and measuring the photocurrent I_{ph} through the solar cell. To facilitate the measurement, light bias and frequency modulations with lock-in amplifiers can be used. When an EQE signal is collected a certain bias voltage is applied to the cell. Therefore, applying a sufficiently large reverse bias voltage can assure that nearly all photogenerated charge carriers in the intrinsic layer are collected. Thus, this measurement can be used to study the optical losses in the overall device stack. It is important to mention that, since I_{ph} is dependent on the bias voltage, the bias voltage must be fixed during measurement. Figure 1.9 shows the EQE signal for a high-quality crystalline silicon solar cell. A signal close to one means that

almost every photogenerated carrier is successfully collected. On the contrary, recombination, reflection, or parasitic absorption losses lead to a lower EQE signal. In the case of crystalline silicon, it becomes transparent for long wavelengths because the penetration depth exceeds the optical thickness of the absorber, therefore most of the light leaves the solar cell before it can be absorbed.

If we perform the EQE measurement under short circuit conditions (when a bias voltage of 0 V is applied) the measurement can be used to determine the short circuit current density Jsc. Determining Jsc via the EQE has the advantage that it is independent of the spectral shape of the light source used, in contrast to determining the Jsc via a J-V measurement. Secondly, when performing a J-V measure, to ensure the desired active area, a shading mask is used. This means that the current evaluation might be subjected to a certain error aroused by how the mask is placed/evaluated. The EQE measurement is independent of the active area, hence, to accurately measure the short circuit current density, a spectral response setup has to be used. For the Jsc determination, we combine the photon flow at a certain wavelength with the EQE at this wavelength, leading to the flow of electrons leaving the solar cell at this wavelength. Jsc is then obtained by integrating across all the relevant wavelengths.

$$J_{sc} = -q \int_{\lambda_1}^{\lambda_2} EQE(\lambda) \; \Phi_{ph,\lambda}^{AM1.5} d\lambda \qquad (1.11)$$

Where $\Phi_{ph,\lambda}^{AM1.5}$ is the spectral photon flux.

Losses mechanisms

Once discussed the working mechanism and the fundamental parameters that govern a solar cell, the loss mechanisms knowledge is another fundamental step to fully understanding how to improve the photovoltaic performances. Differently from the optical losses (which concern the probability of absorbing a photon, the reflection losses, and the parasitic absorptions) we now discuss the recombination mechanisms that affect the photo-generated carriers. As already mentioned, not every photo-generated carrier is successfully collected, because of recombination processes, which can be subdivided into two major classes, radiative e nonradiative. Each recombination process is characterized by a recombination rate R_i and the overall recombination rate is given by the sum of them. Hence, the total lifetime is related to the lifetimes of the different processes via equation 1.12.

$$\frac{1}{\tau_{tot}} = \frac{1}{\tau_1} + \frac{1}{\tau_2} + \cdots \qquad (1.12)$$
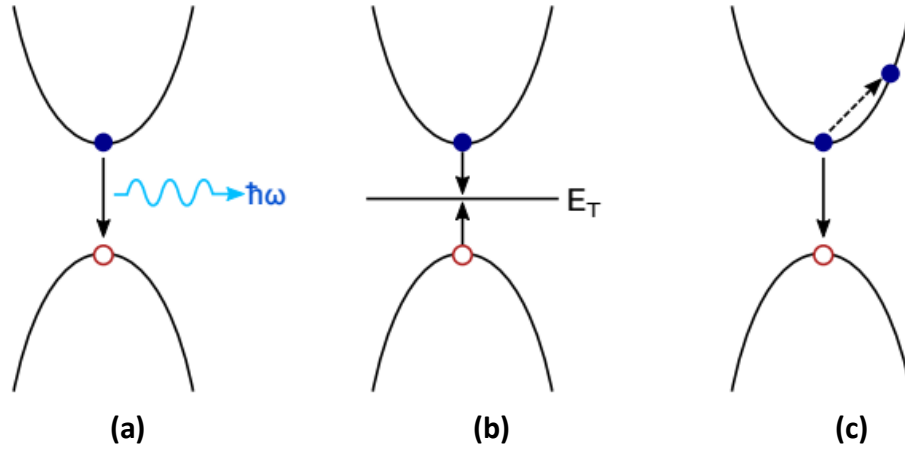
Figure 1.10: Schematic representation of the losses mechanisms in a solar cell: (a) radiative recombination, (b) RSH recombination, and (c) Auger recombination.

The more recombination mechanisms are present, the shorter is the overall lifetime of the excess minority carriers. When illuminated, excess electrons and holes are created. As the electron and hole concentrations increase, the recombination rate will also increase. At some point, the generation and recombination rates will be the same. Under this assumption is possible to determine the minority carrier's lifetime in an n- and p-type semiconductor (equation 1.13 and 1.14 respectively).

$$\tau_{pd} = \frac{1}{\beta n_0} \qquad (for\ holes\ is\ the\ n-type\ SC) \ (1.13)$$

$$\tau_{nd} = \frac{1}{\beta p_0} \qquad (for\ electrons\ is\ the\ p-type\ SC) \ (1.14)$$

where n_0 and p_0 are the equilibrium concentrations.

Another recombination process is the Shockley–Read–Hall (SRH) recombination process. This process is facilitated by an impurity atom or lattice defect, whose concentration is usually small compared to the acceptor or donor ones. These recombination centers introduce allowed energy levels (E_T) within the forbidden gap, so-called trap states. An electron can be trapped at such a defect and consequently recombines with a hole that is attracted by the trapped electron. In this case the recombination is typically non radiate, and the excess energy is dissipated into the lattice in the form of heat. However, this process seems to be less probable compared to the other recombination processes.

The lifetimes' expressions are as follows

$$\tau_{p,RSH} = \frac{1}{c_p N_T} \qquad and \qquad \tau_{n,RSH} = \frac{1}{c_n N_T} \qquad (1.15)$$

Where c_p and c_n are capture coefficients for holes and electrons, and N_T is the trap density. Therefore, for a good semiconductor device, it is crucial to keep N_T low.

Another recombination path that is typical of indirect bandgap materials, like silicon, is the Auger recombination, which is a three-particle process. The momentum and energy of the recombining hole and electron are conserved by transferring energy and momentum to another electron (or hole). If the third particle is an electron, it is excited into higher levels in the electronic band. This excited electron relaxes again, transferring its energy to vibrational energy of the lattice, or phonon modes, and finally heat. Similarly, if the third particle is a hole, it is excited into deeper levels of the valence band, from where it rises back to the valence band edge by transferring its energy to phonon modes.

Auger recombination strongly depends on the charge carrier densities of electrons and holes, as seen from the square dependence in the definition of their lifetimes,

$$\tau_{eeh} = \frac{1}{C_n N_D^2} \qquad and \qquad \tau_{ehh} = \frac{1}{C_p N_A^2} \qquad (1.16)$$

Where C_n and C_p are proportionality constants that are dependent on the temperature. From figure 1.10 we can see a schematic representation of the different losses mechanisms described so far and considering the described recombination mechanisms equation 1.12 can be written as follows.[10]

$$\frac{1}{\tau^{tot}} = \frac{1}{\tau^{Auger}} + \frac{1}{\tau^{radiative}} + \frac{1}{\tau^{SRH}} \qquad (1.17)$$

Coupled with these efficiency's detrimental mechanisms, another intrinsic loss needs to be taken into account, namely the spectral mismatch. As already mentioned, only photons with energy hv greater than the material's energy gap can be absorbed and generate an electron-hole pair. Moreover, electrons and holes tend to occupy energy levels at the bottom of the
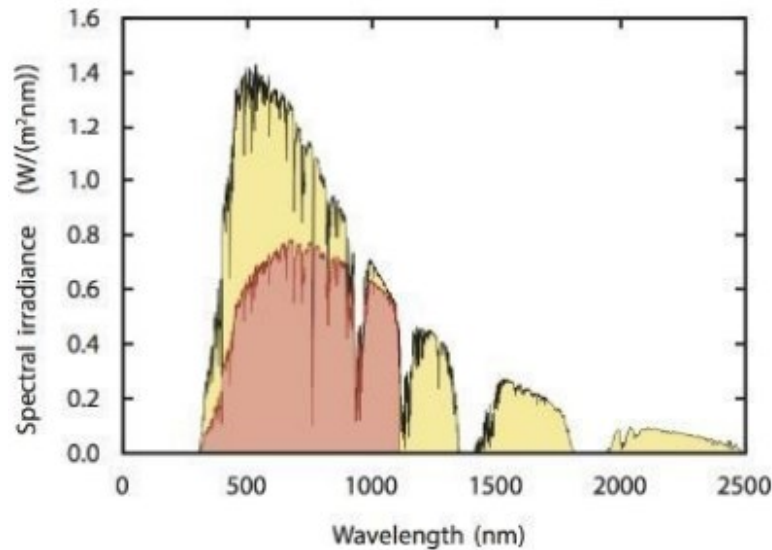

Figure 1.11: AM1.5G spectrum (yellow) and the fraction of the AM1.5 spectrum that can be converted into usable energy by a crystalline silicon solar cell.

CB and the top of the VB, respectively, thus when an electron (or hole) is promoted to an energy level higher in energy compared to the CB edge (or deeper in the VB), the excess energy is released as heat into the semiconductor lattice. This process is known as "thermalization". Because of these two major limitations, only a portion of the full AM1.5G spectrum can be harvested. Figure 1.11 clearly shows in the case of crystalline Silicon, the amount of unexploited spectrum.

Schockley Queisser limit

There is a theoretical limit for a solar cell efficiency based on a single photo-absorbing material. In 1961 William Shockley and Hans J. Queisser proposed a new theoretical upper limit for the efficiency of solar cells employing p-n junctions in semiconductors (the so-called SQ limit). They state that "this limit is a consequence of the nature of atomic processes required by the basic laws of physics, particularly the principle of detailed balance".[11] Before that time only "semiempirical limits" have been evaluated, thus SQ imposed the theoretical threshold for single active absorber material solar cells (also called single-junction solar cells). The comparison between the limit and the semiempirical one is shown in figure 1.12.

They state that the efficiency is limited by the energy gap of the active material and the number of radiative recombination. This means that, if the radiative recombination is only one of the recombination mechanisms that occur in the cell, then the efficiency upper limit is further reduced.
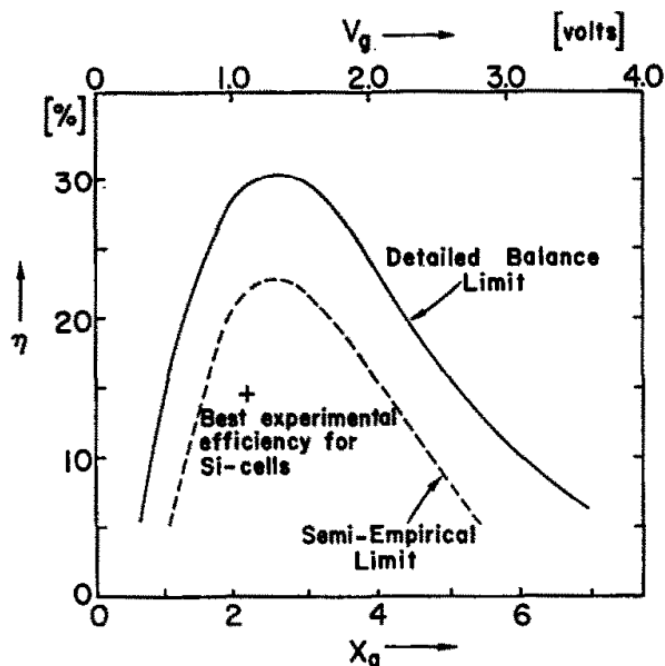

Figure 1.12: Comparison of the "semiempirical limit" of efficiency of solar cells with the "detailed balance limit" (full line), and the "best experiment efficiency at that time for silicon cells" (dashed line).

Three are the assumptions that SQ imposed to investigate the detailed balance limit. First, each photon with energy greater than $h\nu_g$ produces one electronic charge q at a voltage $V_g = h\nu_g/q$. Second, recombination paths other than the radiative ones do not occur. Third, all the photoexcited electrons are extracted from the conduction band, and those that have extra energy thermalize at the conduction band edge. Therefore, the electrical power output divided by the incident solar energy irradiating the cell defines the efficiency as follows:

$$\eta = \frac{I[V(max)]V(max)}{P_{inc}} \qquad (1.17)$$

With equation 1.17 the maximum possible efficiency is around 30%. Nowadays the most efficient solar cell based on a single photo-absorber (also called single-junction solar cell) is based on GaAs $\eta = 29.1\%$ (Alta device), while crystalline silicon (c-Si) achieved a record efficiency of 26.6% (Kaneka). The best performance obtained for a perovskite device is 25.7%. (UNIST), and lower CGIS (23.4%, Solar frontier) CdTe (22.1% First Solar), and organic photovoltaics (city UHK)[12]. The gap between the SQ limit and the real technology arises because a real device must deal with issues that induce optical and electrical losses. Different approaches have been developed to overcome this limit, such as hot carrier conversion, quantum confinement, multiple exciton generation, up and down conversion.[13–16] However, a more promising technology caught the community's attention over many years: the idea of combining multiple photo-absorbers in a multijunction solar cell.

Multijunction and tandem technology

As we cited previously, different approaches have been explored to overcome the SQ limit. Of course, to be competitive with fossil fuels these technologies must have different fundamental characteristics such as being cheap and large-scale manufacturability. Among these, the tandem, or in general, the multijunction technology is the relatively easiest approach that allows exceeding these limits. Figure 1.13 shows the World record efficiencies reached so far by the different technologies in comparison with the SQ limit. The amount of work done per photon could be increased if photons of different energies could be absorbed preferentially in cells of different band gaps. If the solar spectrum could be split up and channeled into different active materials, then it could be possible to avoid any thermalization related losses. A multi-junction cell consists of different active materials (with different bandgaps) each employed in a different solar cell (i.e. junction) while being stacked onto each other. The top cell (the junction firstly facing the sunlight) must have the widest bandgap and will absorb and convert the short wavelength (for example the blue light) radiation. Light with wavelengths longer than the top cell photo-absorber can traverse the top cell and be absorbed in the cells with lower bandgaps below. The bottom cell has the lowest bandgap and absorbs the long wavelength radiation (red and near-infrared light). A schematic example of a triple-junction (therefore, three photo-absorbers) solar cell is shown in figure1.14a and, as we can see from figure 1.14b each cell will absorb a different portion of the spectrum avoiding the spectral mismatch condition, drastically reducing the thermalization losses. On the other hand, increasing the number of layers means also increasing the cost and the complexity of the system. Made of just two active absorbers layers, tandem solar cell is the promising technology that can meet all these requirements. The two subcells are arranged one after the other, and competitive absorptions must be avoided. Ideally, no absorption overlap should be present between the two active materials,
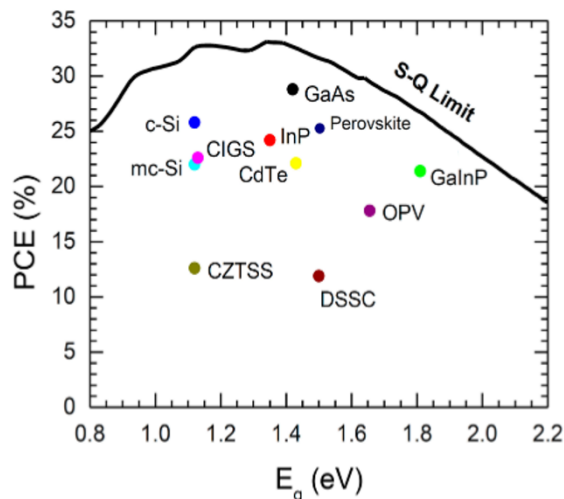

Figure 1.13: Actual PCE World record for different single-junction solar cell technologies.
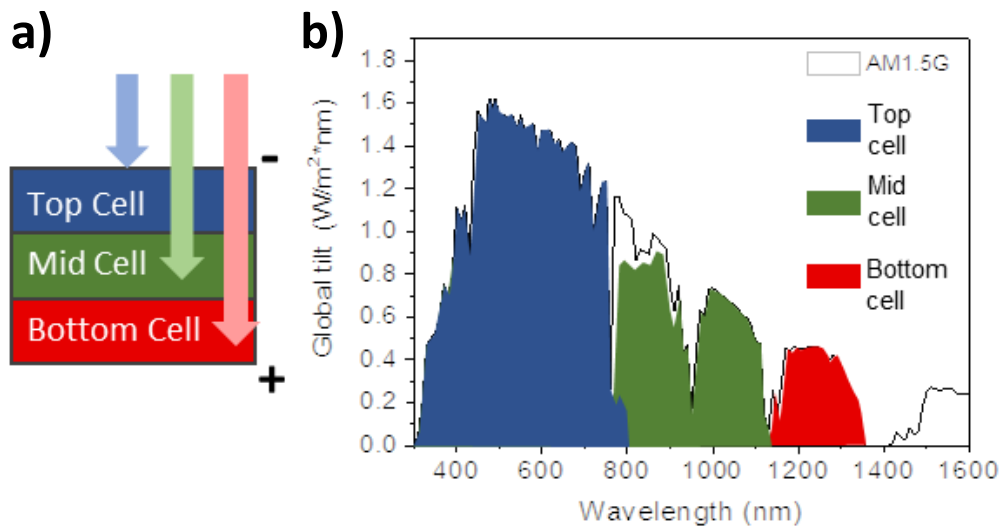
Figure 1.14: (a)Schematic representation of a triple-junction solar cell and (b) portion of the spectrum absorbed by each subcell.

meaning that each sub-cell can efficiently harvest different wavelengths of the incoming light. The tandem configuration can be realized in different ways, but the most meaningful are the so-called two- and four-terminal configurations (figure 1.15 a and b respectively).[17] In the four-terminal (4T) configuration the subcells are produced and connected independently, while in the two-terminal monolithic configuration (2T), two subcells are connected in series via a recombination layer. Considering the latter one, the Voc is the sum of the respective top and bottom Voc's, and the final current density is the lower value between the two subcells' Jsc. Therefore, to exploit the maximum power output from the device, the "current match" condition must be satisfied, hence the same amount of current density needs to be delivered by the two subcells. Conversely, in the 4T tandem, the two subcells work independently, thus, the current match condition is not necessary, but independent electrical contacts to top and bottom cell, which is practically hard to achieve and more expensive. Moreover, each cell needs to be encapsulated, therefore the light would pass through a larger number of layers increasing the losses due to optical effects.
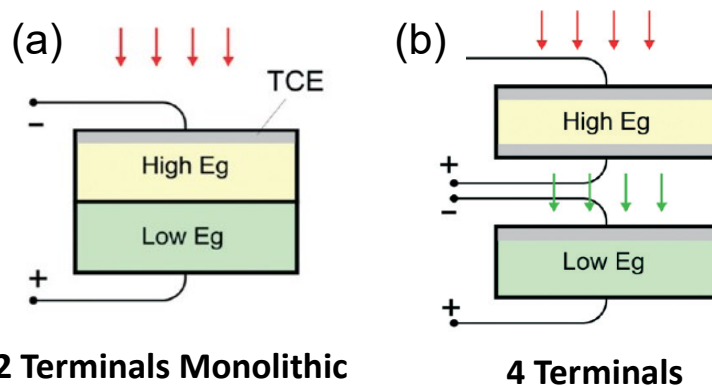

Figure 1.15: (a) 2 Terminal monolithic and (b) 4 terminal tandem configurations. [17]

A comparison between the advantages and disadvantages of the 2T and 4T tandem technology is provided in the following table.

	2T tandems	4T tandems
Fabrication	Complex, requires a recombination junction between the sub-cells and processing compatibility in terms of temperature, solvents, etc.	Simple, the two sub-cells can be fabricated independently and then stacked
Performances	Top performances, minimal losses. Requires the current matching condition for optimal performances.	Serious optical losses due to the stacking that induces unwanted reflections. Does not require the current matching condition, the two cells can operate independently.
Manufacturing	Monolithic integration, depending on the technology can be an advantage in large production lines	Benefits for small businesses that cannot afford large production lines
Costs	Based only on the bills of materials used.	Very high costs for the balance of the system. Requires twice the length of the cables and two sets of inverters. Double the weight due to multiple glasses. Not suitable for utility-scale

Table 1. 1: Comparison between the two different architectures.

For clarity, in this work, we focus on monolithic 2T configuration.

Crystalline silicon cells

Thanks to its stability, low cost, and relative ease of manufacturing crystalline silicon (c-Si) is the dominant technology in the PV market, and it will likely continue its dominance in the next years. The success is also attributed to the continuous reduction in manufacturing costs.[18] Such a reduction is utterly due to the decline that polysilicon (the raw material for the fabrication of PV modules) has experienced over the last 15 years. Until the last two years, most of the c-Si PV production capacity is vested in the fabrication of aluminum back surface field (Al-BSF) cells, in which the entire silicon rear surface is alloyed with aluminum, while the p-n junction is obtained through the diffusion of phosphorous (n-type) in boron-doped p-type silicon wafers. As figure 1.16 shows, only five
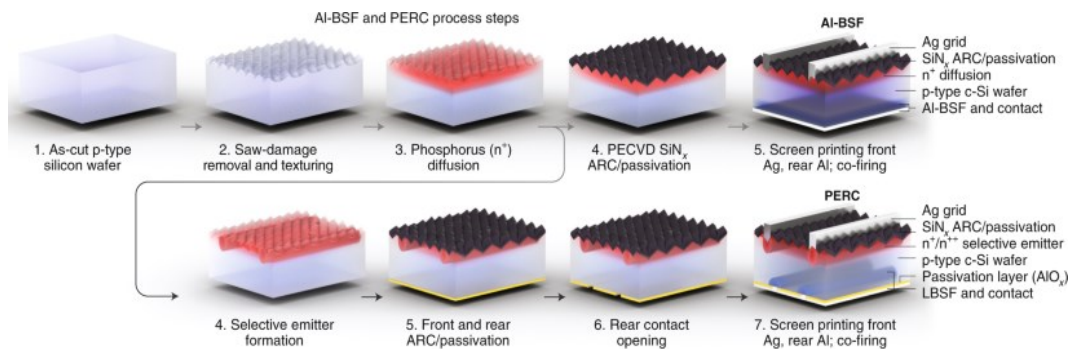

Figure 1.16: Fabrication process of Al-BSF and PERC solar cells.

main fabrication steps are required to produce this cell's design (texturing; front phosphorus diffusion; silicon nitride, SiNx, deposition; screen printing, and co-firing of the metal electrodes). However, this cell structure has a practical upper limit around 20% PCE, well below the theoretical SQ limit. An evolution of the Al-BSF technology is represented by the PERC (passivated emitter and rear cell) configuration. PERC devices are manufactured in a similar way to the Al-BSF cell but with rear-surface passivation (often aluminum oxide, AlO_x) and localized aluminum BSF contacts (typically defined by laser ablation of the AlO_x layer). In this way, the oxide passivated rear-contact increases the device voltage compared to the full-area Al-BSF cell. Nowadays, PERC cells have a practical PCE efficiency of around 22-23% at the production line, with record PCE of 25% for lab scaled devices. For both technologies, the direct application of the contacting metal onto the active layer leads to defect-assisted Shockley–Read–Hall contact recombination losses, at the silicon-metal interface, due to the high density of electronically active states which present an energy that lays within the silicon bandgap.[19] Sandwiching the silicon wafer between passivating thin films (commonly silicon oxide, SiO_x, or hydrogenated amorphous silicon, a-Si:H) allows to reduce these recombination losses. This relatively simple passivating contacts device design is called silicon heterojunction cell (SHJ). However, to benefit from this passivation, the p-n junction must be realized, outside of the c-Si absorber, using doped layers of amorphous silicon (either n-type n-Si:H, or p-type p-Si:H amorphous silicon). Due to the low lateral conductivity of these doped amorphous silicon layers, a transparent conductive oxide (TCO, typically, sputtered indium tin oxide, ITO) provides lateral charge transport to the screen-printed metal fingers and acts as the anti-reflective coating (ARC, similarly to the SiN_x for the PERC al Al-BSF configurations). Figure 1.17 describes the fabrication process of SHJ. The most critical performance limitation of this design is the parasitic absorption in the front TCO and a-Si:H layers. Another cell design, the so-called interdigitated back contacted (IBC) architecture, where the contacts are placed on the rear side of the wafer, is a solution to this. On the other hand, the increase in fabrication complexity, and the re-design of the front contacts to the rear side of the cell, requires more strict process conditions on both the electron and hole contact resistivities owing to their relative reduction in surface area (typically these extra steps include complicated photolithography processes, etching processes, and selective depositions). In addition, most of the excess majority carriers are photo-generated at the
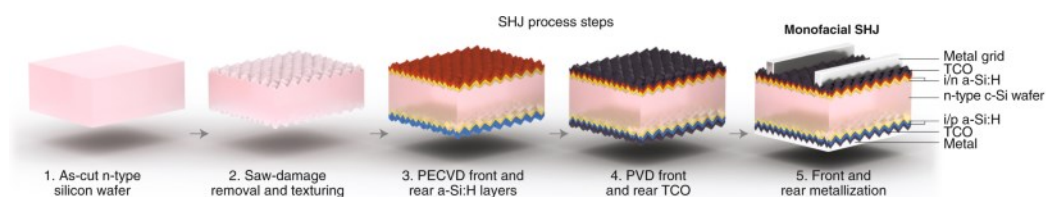

Figure 1.17: Fabrication steps of a Silicon heterojunction solar cell.[19]

front of the wafer therefore high bulk lifetimes and state-of-the-art surface passivation is mandatory to achieve the long diffusion lengths needed to maintain a high quantum efficiency. For these reasons, the IBC configuration covered only a minor part of the PV market, leaving most of it to the Al-BSF first, and to the PERC configuration later: However, this trend is swiftly changing. The constant development of the silicon heterojunction is threatening the domain of the so-called diffused junctions (PERC and Al-BSF). Therefore, it will not be surprisingly if, the next five or ten years, the silicon heterojunction will take over in the PV market similarly to the mono-crystalline in the last five years.

Perovskite

With the name perovskite, a wide class of materials is indicated. Historically, perovskite was first discovered in a piece of chlorite-rich skarn by the Prussian mineralogist Gustav Rose in 1839.[20] It was a $CaTiO_3$ mineral, and it was named after the renowned Russian mineralogist Count Lev A. Perovskiy. Many inorganic metal oxides, such as $BaTiO_3$, $PbTiO_3$, $SrTiO_3$, etc., were found to have the perovskite structure. Therefore, perovskite materials are more commonly known as metal oxide, and nowadays they are used in various ferroelectric, dielectric, piezoelectric, and pyroelectric applications. But except for some limited composition, oxide perovskites do not exhibit good photovoltaic properties that would make them suitable for solar applications. However, a class of halide perovskites, in which halide anions replace the oxygen in the crystalline structure, shows the semiconducting properties that are desired for PV application. The chemical formula that distinguishes perovskites is ABX_3, in which A and B are cations and X is an anion. In an ideal cubic structure, the B cation has a 6-fold coordination, surrounded by an octahedron of anions, while the A cation has a 12-fold cuboctahedral coordination. As figure 1.18 shows the cubic unit cell is composed of A cations at the cube corner positions, B sitting at the body-center position, and X anion occupying the face-centered positions.
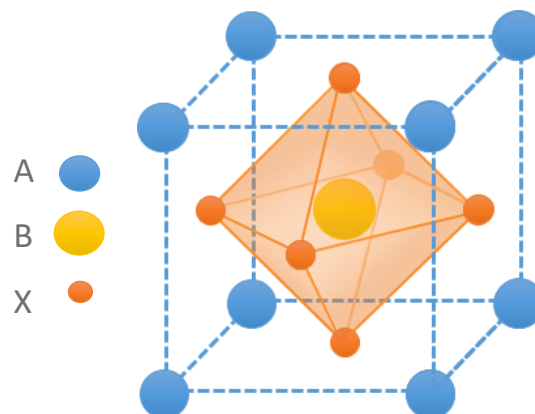

Figure 1.18: Perovskite unit cell structure.

The journey of perovskite as photovoltaic material started in 2005 when Akihiro Kojima, a graduate student at Tokyo Polytechnic University, joined the research group led by Tsutomu Miyasaka to learn experiments on dye-sensitized solar cells (DSSCs). This study aimed to examine the possibility of using halide perovskites as a sensitizer on mesoporous TiO_2 electrodes. The adopted perovskite composition was $CH_3NH_3PbX_3$ (A= $CH_3NH_3^+$ B= Pb^{2+} and X = I^-, Br^-) and it was used as sensitizer on the TiO_2 mesoporous electrode with a lithium halide-containing electrolyte solution to close the circuit.[21] With the assumption that perovskite would have worked as a quantum dot-like sensitizer and with the aim of covering a large surface area of thick TiO_2 layer, the halide perovskite precursor was deposited by spin coating, adjusting the loading in order to obtain the layer as thin as possible. As a result in 2009 a 3.8% PCE perovskite based solar cell was fabricated. With this architecture, the main issue was the dissolution of the perovskite into the liquid electrolyte, showing the necessity of a solid-state hole transporter (HTM). Indeed, in 2012, with the collaboration between Henry Snaith's group (in particular Michael Lee, a Ph.D. student in his group) and Miyasaka's group, a solid hole-transport layer called spiro-OMeTAD (2,2',7,7'-tetrakis (N, N-dimethoxyphenylamine)-9,9'-spiro-bifluorene) was used to fabricate the first perovskite based solar cell with a PCE of 10.9%.[22] The higher PCE is attributed to the adoption of an Al_2O_3 mesoporous structure, instead of the previously employed TiO_2. The great innovation was the fact that the dielectric scaffold of Al_2O_3 proved that the perovskite was not acting only as sensitizer, but actually as a proper absorber, including an ambipolar charge transport. Indeed, a cell using this material exhibited higher voltage and PCE, a sign of the long diffusion length of carriers in the perovskite. Thanks to this approach a new class of PV devices was born with the name of meso-superstructured solar cells (MSSC). Snaith et al. also investigated the influence of removing the mesoporous scaffold. They found that the device with no alumina, i.e., a
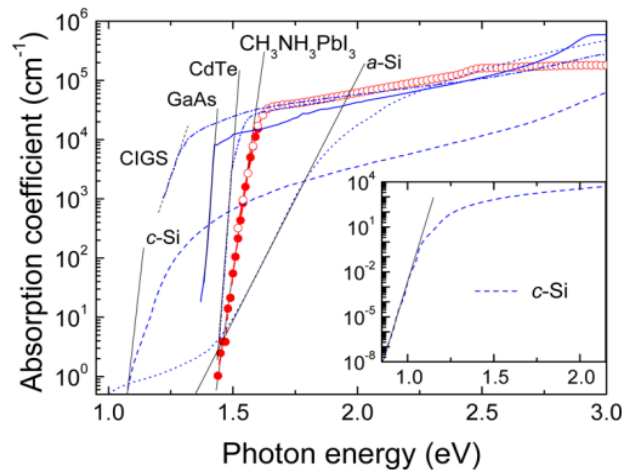

Figure 1.19: Effective absorption coefficient of a CH3NH3PbI3 perovskite thin film (highlighted in red) compared with other typical photovoltaic materials such as, amorphous silicon (a-Si), GaAs, CIGS, CdTe and c-Si.[25]
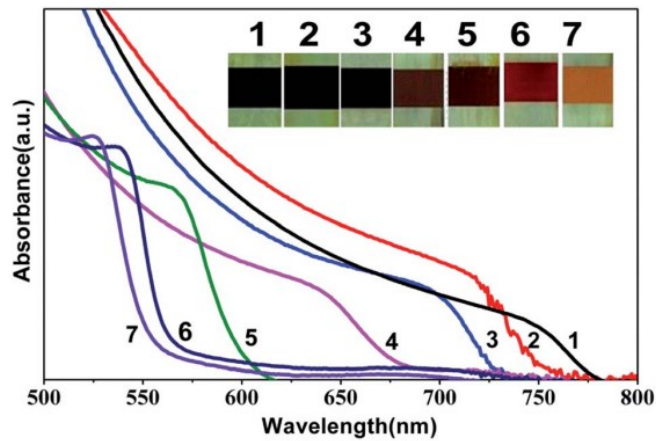
Figure 1.20: *UV-Vis absorption spectra of different halide lead perovskite films. The numbers 1-7 correspond to the different iodide/bromide compositions.*[28]

simple solid thin-film of perovskite sandwiched between the n- and the p-type extraction layers, presented a remarkable high photocurrent illustrating efficient charge generation and ambipolar charge-transport of both electrons and holes through the thin solid perovskite film.[23] This architecture is nothing more than a p-i-n heterojunction solar cell, where the intrinsic layer (i) is the perovskite absorber. These important findings classified the halide perovskite technology among the thin film photovoltaics (together with CIGS and CdTe) and not as DSSC's anymore. After that, Liu et al. proved that vacuum deposition was an alternative to depositing perovskite from solution, by co-evaporating methylammonium iodide and $PbCl_2$ on a compact TiO_2 to form a 300nm thick perovskite with 15.4% efficiency solar cell. [24]

From there, different materials and different perovskite compositions have been studied, pushing the PCE over 25% also thanks to its extremely favorable physical and chemical properties. Figure 1.19 shows the plot of different semiconductors' absorption coefficients with in red the one belonging to a perovskite film with chemical composition described by the formula $CH_3NH_3PbI_3$. The unusual sharp steep of the absorption coefficient at its band gap value (1.57eV), explains why very thin absorbers film (500 to 1000nm) are sufficient to harness most of the incoming light.[25] As we already mentioned, the presence of defects can generate traps levels within the bandgap leading to non-radiative recombination pathways, and hence, decreasing the photogenerated charge collection efficiency. But, unlike other ionic semiconductors, defects in halide perovskites (such as $MAPbI_3$) generate trap states that either reside within the bands (VB or CB) or exist as shallow traps near the CB and VB. Carriers trapped in shallow defects can easily escape and contribute to the current generation. Therefore, the defect-tolerant nature of halide perovskite is reflected by the large carrier diffusion lengths, measured over the PL lifetime, which range from 1 μm (polycrystalline film) to over 100 μm (single crystal).[26,27] This high defect tolerance is also reflected in reduced Voc losses. Indeed, similarly to III-V semiconductors, halide

perovskites have Voc that are very close (up to ~ 0.4V) to the bandgap. Another characteristic that makes halide perovskite widely used is the band gap tunability. Different chemical compositions correspond to different bandgap values. This property can be controlled via tailoring the halogen composition or modification of the A-site cation. For example, it has been shown that considering the absorption spectra of $MAPb(I_{1-x}Br_x)_3$ with $0 \leq x \leq 1$ (thus different values of Br content), the onset of the absorption band shifts to lower wavelength with increasing the Br content in the precursor solution (figure 1.20).[28] The possibility of having different bandgaps makes perovskite an ideal partner for tandem applications, in particular with Silicon, whose bandgap (1.12eV) made difficult the choice of the right partner. To better understand the potential of tandem application figure 1.21 shows the bandgap correlation between the top cell and the bottom cell compared with the overall tandem efficiency. Considering c-Si, in order to have the highest possible efficiency of the tandem solar cell, the bandgap top cell must be around 1.7eV. Halide perovskite is the only material with such bandgap, thus making it the perfect partner for tandem architecture.
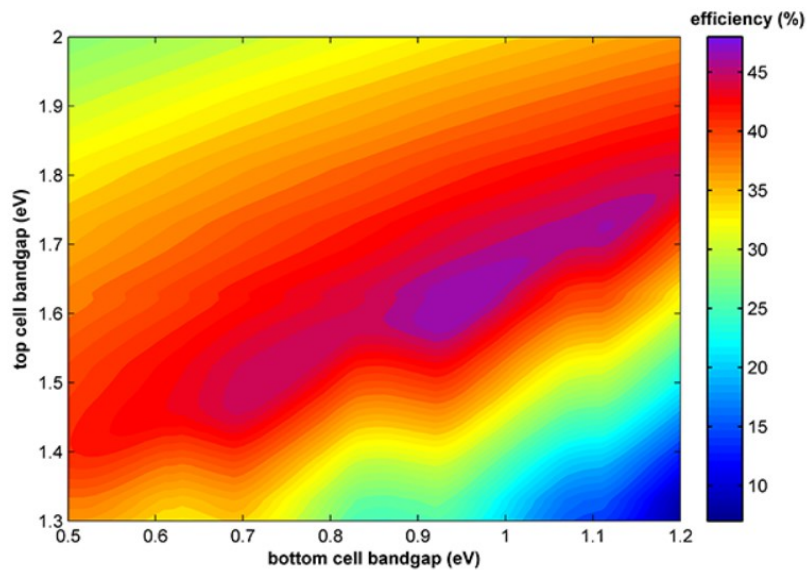
Figure 1.21: Band gap correlation diagram for tandem solar cells.

The transition from single cell to solar module

The term solar module, also called PV module, refers to a series of solar cells that can be connected in different ways and used to exploit the conversion of light into electricity. Usually, the cells are connected to each other in series, forming a so-called "string", then the strings are connected in parallel to each other. Similarly, the modules can be connected in series or in parallel, depending on the requirement of the installation. Over the last decade, the c-Si solar modules efficiency improvement is also attributed to the evolution

of the module design.[29] Moreover, several companies are providing more than 25 years of warranty, and some even aim at 50 years.[30,31] To ensure such a long lifetime, the module configuration and the choice of the materials are crucial. Commercially, there are two module configurations: the single cells module and the thin-film modules. Single cell modules are typically crystalline silicon modules. Here, each single cell is interconnected with the neighbor cell according to the module design, To this category belong c-Si modules (both mono- and multi-crystalline), the expensive III-V modules, and the perovskite-silicon tandem modules. The thin film category exploits a single cell of large area (>1m^2) patterned first in multiple single cells and then interconnected top to bottom. These modules are usually directly fabricated on glass substrate, which is the flipped up-side-down to face the sunlight. To this category belongs the amorphous, the CdTe modules, the CIGS modules, the perovskite single junction and the organic photovoltaics modules. In this thesis when discussing the module fabricating and testing, we will refer only to the single cell configuration.

The most widely used solar module's layer stack for perovskite/silicon tandem is shown in figure 1.22 and the major components are described in the following list:

- Soda-lime glass, several millimeters thick, which provides mechanical stability while being transparent for the incident light. Iron can be found as impurity in these glasses. It absorbs part of the incoming light; therefore, its content must be as low as possible. Moreover, the glass must be tempered in order to increase the impact resistance.

- With a process called lamination (further discussed later), the solar cells are sandwiched between two layers of encapsulants. The most common encapsulant employed in c-Si solar cell modules is called ethylene-vinyl-acetate (EVA), which is a thermosetting polymer.

- The back layer, depending on the adopted technology, can be another glass or a composite polymer sheet. It acts as a barrier against humidity and other stresses. A
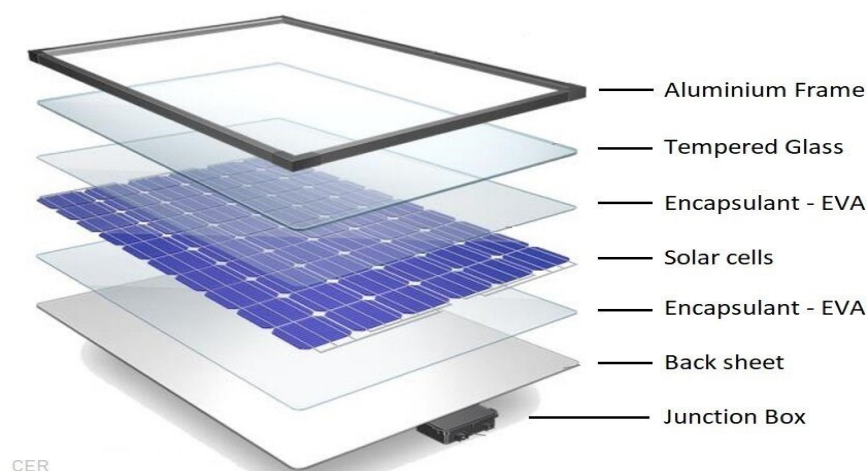

Figure 1.22: Typical c-Si solar module layers' stack.

typical material combination used as back-sheet is PVF-polyester-PVF, where PVF stands for polyvinyl fluoride and, polyester that is often used is polyethylene terephthalate (PET). PET electrically isolates the module while PVF protects the polyester from wind and atmospheric conditions.

- In order to enhance the mechanical stability of the module an aluminum frame is put around the whole module

- Finally, a junction box is placed at the back of the module. In it, the electrical connections to the solar cells are placed and the terminal cables are connected.

As already mentioned, there are many ways in which the solar cells in the module can be connected. Firstly, we can connect them in series. In this way, the total Voc of the string is the sum of the different cell's Voc, while the Jsc is determined by the cell that delivers the smallest current. Secondly, the different cells can be connected in parallel. Now, the total Jsc is given by the sum of the different Jsc while the Voc is the same as for a single cell. Therefore, several strings of series-connected cells can be connected in parallel, or several groups of parallel-connected cells can also be connected in series. In reality, having parallel-connected strings leads to high current and hence increasing resistivity losses in the cables. It is important to mention that on a module level, the considered area is the "total module area", therefore, including the non-active regions, like the spacing between the different cells and the area covered by the interconnections, are taken into account leading to a module efficiency that can be remarkably different from the ideal performance just obtained from the cells composing the module. To this, we add the resistive losses of the soldering and interconnections between cells, the reflection losses induced by the front glass, and the parasitic losses of the encapsulants. All of these losses are commonly referred to cell-to-module losses (CTM) and nowadays can be accounted for 2% of the absolute PCE. The previously mentioned improvements on the module design aimed to reduce these non-active regions, which can be achieved by increasing the size of the modules, the device packing using larger wafers, (half)cut wafers, and shingling approaches.[29] Indeed, a few years ago, a PV module was made with 36 solar cells connected in series, increased to 72 and nowadays up to 96 solar cells are used. In parallel, improvements in the tabbing process and in the soldering minimized the resistive losses and the shadowing of the soldering ribbons. The most efficient solar modules commercially available with conventional silicon solar cells have PCEs between 21.4% and 21.6%, generating 580 W/module; while modules based on interdigitated back-contacted (IBC) cells achieve PCE of 22.8% and power generation of 450 W/module.

Solar angles

The progress made so far, regarding perovskite as a photovoltaic material, highlight the need to study these materials in terms of stability and their behavior under real-world conditions. In particular, the latter one is quite unexplored. Indeed, most of the research at the academic level focuses on improving the performances in lab conditions without considering the real-life application. In lab conditions, the solar irradiation is always constant at 1-Sun and perfectly perpendicular to the device. These conditions are hardly matched in real installation. Therefore, the need to understand not only the physical mechanism that govern the losses in outdoor condition but also the variation of the performances, is mandatory to predict the viability of the technology, looking at a potential commercialization. To understand and analyze this topic, the sun's motion during the day needs to be recalled and, as well, some angles that define its position throughout the day. The sun's position in the sky changes from day to day and from hour to hour. It is common knowledge that the sun is higher in the sky in the summer than in winter. The relative motions of the sun and earth are not simple, but they are systematic and thus predictable. Firstly, we can define the "declination angle (δ)" as the angle between the sun-earth imaginary centerline and the projection of this line on the equatorial plane. It varies during the year due to the tilt of the Earth on its axis, which is 23.45° of rotation, and the rotation of the Earth around the sun. Therefore, this angle seasonally varies from +23.45° on June 22 (summer solstice in the northern hemisphere) to -23.45° on December 21-22 (winter solstice in the northern hemisphere) and it is zero only at the spring and fall equinoxes. Other important angles are, *i* the "solar altitude angle α" (also known as elevation angle) defined as the angle between the sun's ray and a horizontal plane (earth's surface). α is related to the *ii* "solar zenith angle φ", which is the angle between the sun's ray and the vertical line perpendicular to the horizontal plane. At noon the elevation angle is maximum
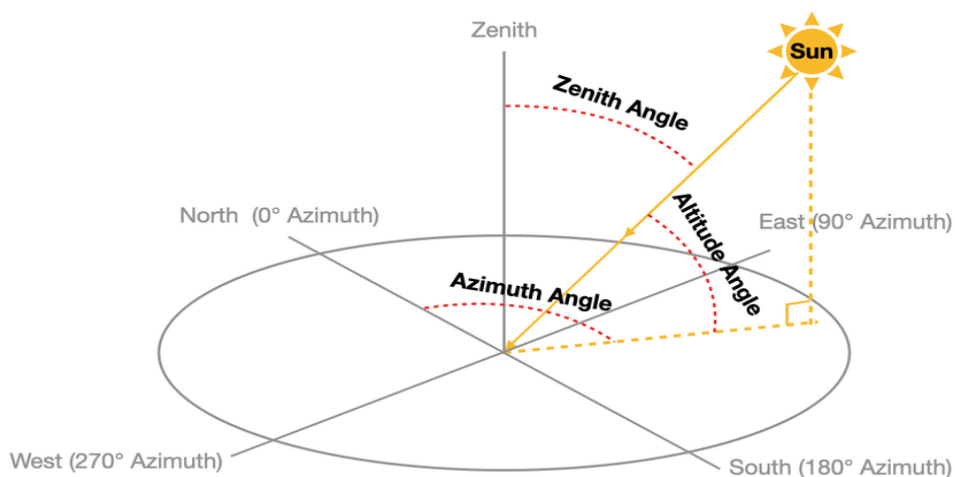

Figure 1.23: Solar angles representation.

while the zenith angle is minimum. *iii* the "solar azimuth angle *z*" is the angle of the sun's rays measured in the horizontal plane from the south direction, for the Northern Hemisphere, or from the north direction for the Southern Hemisphere.[10] The angle between the sun and a fixed location on Earth depends on the particular location (the longitude of the location), the time of year, and the time of day. α and *z* are the two fundamental angles that are used to orient photovoltaic modules. Figure 1.24 shows the so-called polar plot (at the KAUST location of the outdoor testing site[32]), which describes the motion of the sun during the day and throughout the year. The straight lines represent the azimuth angles, which means that when the sun is directly north the azimuth angle is 0° and when it is at the equator *z* is 90°. The concentric circles represent the elevation angle with the outermost circle corresponding to α equal to zero and the center point represents α equal to 90°. The power density, striking the solar panel surface, will always be at its maximum when the PV module is perpendicular to the sun. Obviously, during the year this condition would be satisfied just for few days. Therefore, in order to maximize the power incident on the module surface over the course of the year, the module is tilted by a certain angle, called "tilted angle β" and the maximum power is obtained when β is equal to the latitude of the location. As a result, based on the Earth's location the tilted angle is different.
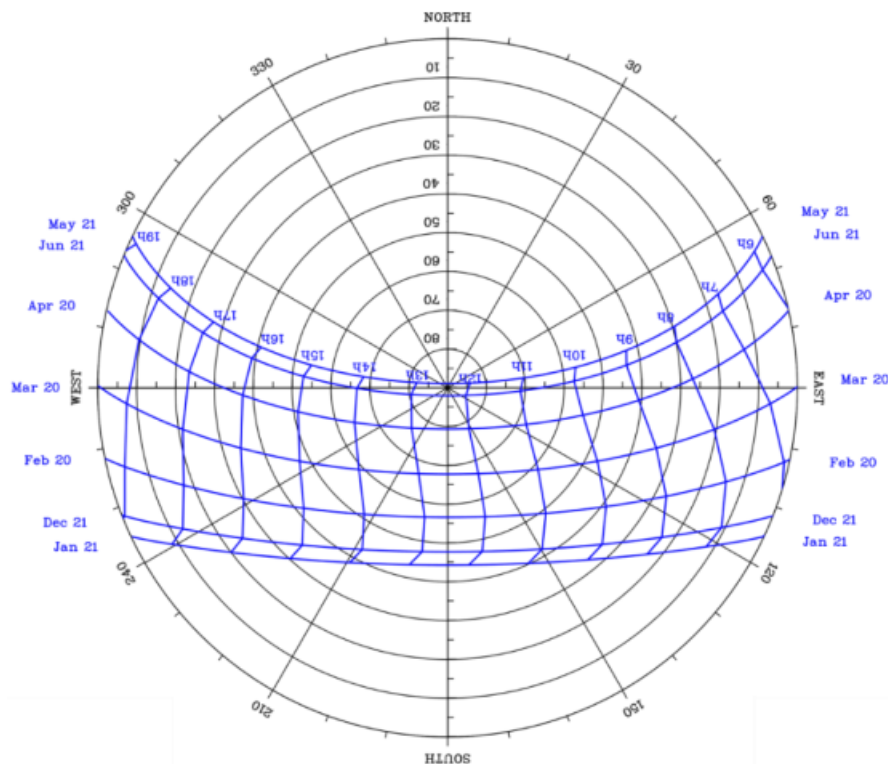

Figure 1.24: Polar plot at the KAUST location outdoor testing site.[32]

Chapter 2

Device fabrication

In this chapter, we will describe the different steps to fabricate our two-terminal monolithic tandem minimodules, starting from the cell's fabrication and ending with the encapsulation process. Moreover, the characterization set up, will be also discussed.

Silicon bottom cell

For the silicon heterojunction bottom cell's fabrication: 4-inches double-sided polished wafers (float-zone, TOPSIL, n-doped, resistivity 1–5 Ωcm^{-1}, and thickness 250–280μm) were used as starting point. The wafers were purchased double-side polished. The polished surface induces reflection losses and therefore decreases the photoconversion efficiency. In order to reduce this detrimental effect, on the wafer's surfaces, a randomly textured pyramids structure was obtained using an alkaline solution. The pyramids' size is controlled by interchanging the temperature, the alkaline concentration, and the processing time of the texturing process. To further improve the quality of the texturing, an additive was added during the process. The texturing process is based on the etching of the silicon atoms along the (100) direction, which have a weaker bonding compared to the atom in the (111) direction. For this reason, the pyramids are all equally distributed with an angle of 52°. The texturing process was followed by a cleaning step RCA procedure. In this step, the wafers are cleaned in two solutions, RCA1 and RCA2. RCA1 is used to remove organic contaminants, by oxidation of the wafer surface in an NH_4:H_2O_2:H_2O solution at 75°C. The

ITO (15 nm)
nc:Si-H(n) (6nm)
a:Si-H (i) (8nm)

Silicon

a:Si-H (8nm)
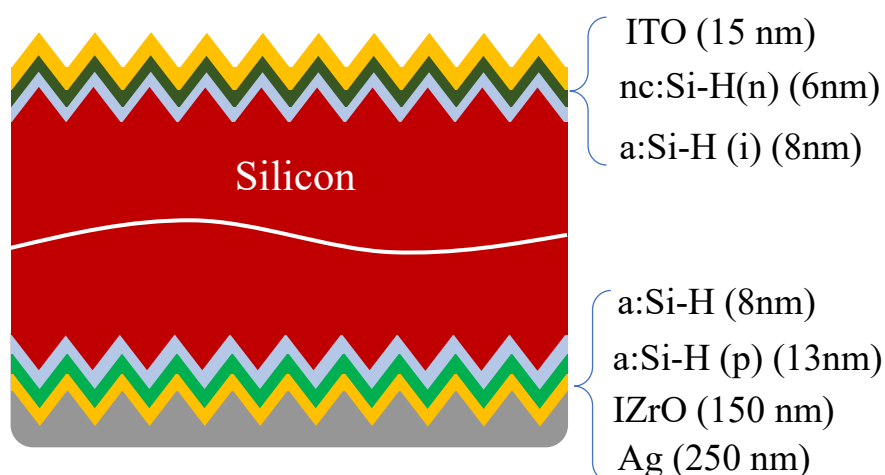a:Si-H (p) (13nm)
IZrO (150 nm)
Ag (250 nm)

Figure 2. 1: *Silicon bottom cell device stack representation. The n-type doped amorphous silicon includes a nanocrystalline component, therefore represented as nc.*

RCA1 oxide layer is then removed in a hydrofluoric acid (HF) solution at 5%. After RCA1, RCA2 is used to remove metal contaminants, again by oxidation of the wafer surface in an HCl:H_2O_2:H_2O solution at 75°C. Finally, a second HF solution at 5% is used to remove the RCA2 oxide layer. In between the steps, the wafers are rinsed thoroughly with DI water. This process is commonly known as "wet processing". After the we process the surfaces of the wafers were passivated by the deposition of intrinsic (i) amorphous silicon (a-Si:H) followed by amorphous and nanocrystalline doped layers (p and nc-n with thickness of 12 and 40nm, respectively) deposited in the PECVD/PVD cluster, Octopus2 from Indeotec. The deposition of these layers in done via a well-optimized recipe that uses silane, phosphine, and trimethyl borane (TMB) as precursor gases, combined with argon and hydrogen during the deposition process. To create the rear contact, Indium doped Zirconium oxide (IZrO) and Ag were sputtered on the rear side (150nm and 250nm, respectively). At the front, for the recombination junction, 15nm of ITO were sputtered in the Octopus2 cluster. Figure 2.1 shows the bottom cell's layer stack.

Perovskite top cell

Once the silicon bottom cell is fabricated, the different top cell layers are deposited for the realization of the perovskite/silicon tandem. In this work we opted for the so-called p-i-n configuration, in which electrons from the silicon are recombining with holes from the perovskite. The opposite configuration is also possible, but less efficient and of more complex fabrication. In the p-i-n configuration (also called inverted structure), the n-side of the tandem (also referred to the ETL) is facing the sunlight, while the p-side (the HTL) is facing the ground. For the perovskite top cell fabrication, the hole transport layer (HTL) is the first layer that must be deposited on top of the recombination junction. As HTL, 2PACz [2-(9H-Carbazol-9-yl)ethyl]phosphonic acid (>98%, Tokyo chemical industry), has been utilized, and deposited on the silicon bottom cell, by spin coating at 5000 rpm for 50 seconds, followed by a drying step at 100°C for 10 minutes. The concentration precursor solution was 1mg/mL in ethanol. The 2PACz molecule can covalently bind to the underlying ITO through its phosphonic group, thus forming a conformal self-assembly monolayer.[33] This bond modifies the ITO work function, with the results of inducing a hole selectivity behavior of the TCO layer. It is important to mention that, in order ensure a bond between the phosphonic group and the underneath layer, a UV-Ozone treatment for 900 seconds was carried out before the deposition, which also allows to remove possible impurities and create the carboxylic groups to which the 2PACz can bind.[34] Subsequently,
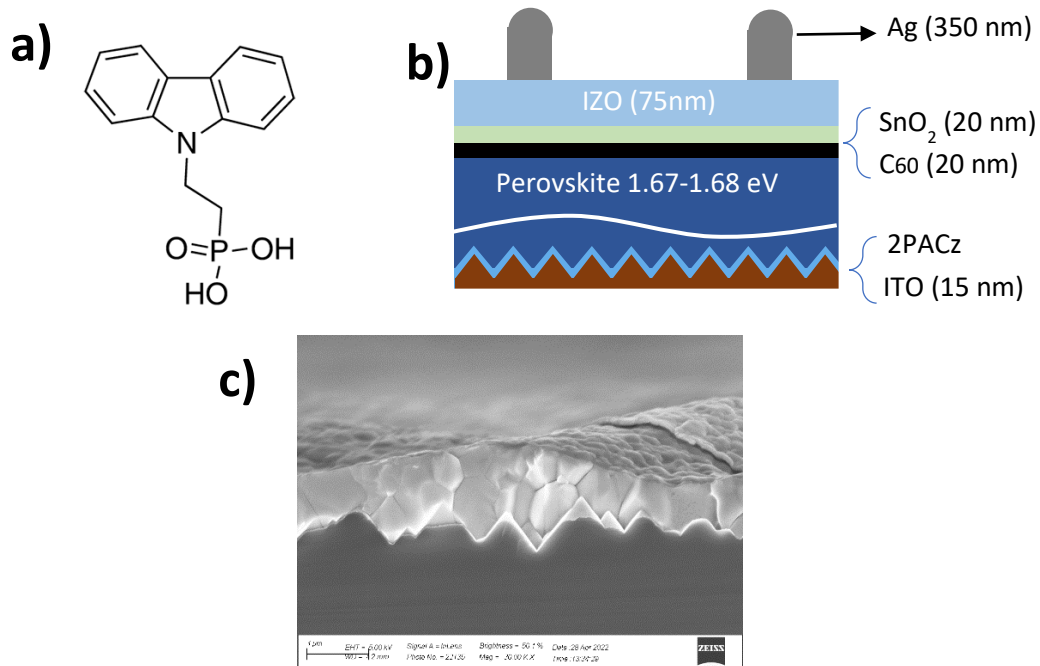
Figure 2.2: *a) Perovskite top cell representation. b) 2PACz molecule. c) SEM cross-section image of the tandem solar cell.*

a 1.7M $Cs_{0.05}FA_{0.8}MA_{0.15}Pb(I_{0.75}Br_{0.25})_3$ perovskite precursor solution was prepared by dissolving a mixture of FAI (Greatcell solar), MABr (Greatcell solar), CsI (99.999% Sigma Aldrich), PbI_2 (99.999%, Alfa Aesar), and $PbBr_2$ (99.999% Alfa Aesar) in a mixed solvent DMF/DMSO 4:1. 75 µL of perovskite solution was spin-coated at 2,000 rpm for 45 s. The long dwell time allows to obtain complete coverage of the perovskite layer on the textured silicon cell. After that, the speed was increased to 7,000 rpm for 8 s. The acceleration from 2000 rpm to 7000 rpm was imposed to be within 2 s. In this acceleration step, 200 µL of chlorobenzene (CB) was dropped in the center of the substrates. Thanks to this step the high boiling point solvent (DMF/DMSO) was extracted, allowing the beginning of the crystallization of the perovskite film. After the deposition, the substrates were transferred onto a hotplate at 100°C for a 15 minutes annealing process. The whole process is done in the nitrogen-filled glovebox. On top of the perovskite, 1 nm of lithium fluoride (LiF) (99.85%, Alfa Aesar) and 20nm of C_{60} (> 99.95% NanoC) were thermally evaporated (Angstrom Evovac). LiF is used as passivating layer, therefore it reduces the concentration of defects at the perovskite surface allowing higher Voc. C_{60} instead, works as electron transport layer (ETL). On top of this contact stack, 20 nm of SnO_x were then deposited by atomic layer deposition (ALD) using a Picosun system. The substrate temperature was maintained at 100°C during ALD deposition with TDMA Sn precursor source at 80°C and H_2O source at 18°C. 150 cycles were used to achieve the final thickness. The SnO_x acts as buffer layer and protects the underlying layers from the kinetic damage of the following sputtering deposition. For the IZO deposition, a 3-inch IZO ceramic target containing 98 wt% In_2O_3 and 2 wt% ZnO was used. Through a shadow mask, 75 nm of IZO was sputtered

on top of the SnO$_x$. IZO is the preferred TCO because it does not require high temperature post annealing treatments, and can be used as deposited. On top the IZO layer, Ag fingers with a thickness of 350 nm were thermally evaporated using a high precision magnetic shadow mask. As final step, 120 nm MgF2 was thermally evaporated as an anti-reflection layer. The evaporation rate and thickness of each deposition were monitored by quartz crystal microbalance sensors.

Minimodule configuration

Due to its stability issues when exposed to atmosphere and relatively high temperatures,[29,35] the module fabrication process required for perovskite/silicon tandem is more challenging compared with single-junction c-Si PV. The lack of stability is one of the main reasons that blocks perovskite to become the predominant technology in the PV field. However, isolating the device inside a module configuration is one way to improve its stability. In general, to obtain the final module, the different layer stack, such as the one presented in figure 1.22, undergoes an encapsulation process. The encapsulation process (further discussed later in this work) is carried out by vacuum lamination: softening, melting, or cross-linking the encapsulant, and sealing the module with temperatures ranging between 100 and 150°C, depending on the technology. Figure 2.3 shows the adopted minimodule configuration, in which the tandem cell is sandwiched between two encapsulant sheets and two standard module glasses with a dimension of 7 x 7 cm and 32 mm of thickness. The encapsulations were done using an industrial vacuum laminator Ecolam 5 Ecoprogetti. In order to seal the cell from the external environment two layers of edge sealing (poly isobutylene, PIB, butyl rubber) are used on the side of the glass. The contacts need to be extracted from the minimodule, and this is done via the so-called tabbing process. In our case, two copper ribbons, covered with a Pb/Sn alloy are placed on the top and bottom contacts utilizing a silver paste. To ensure a proper connection and eliminate the solvents
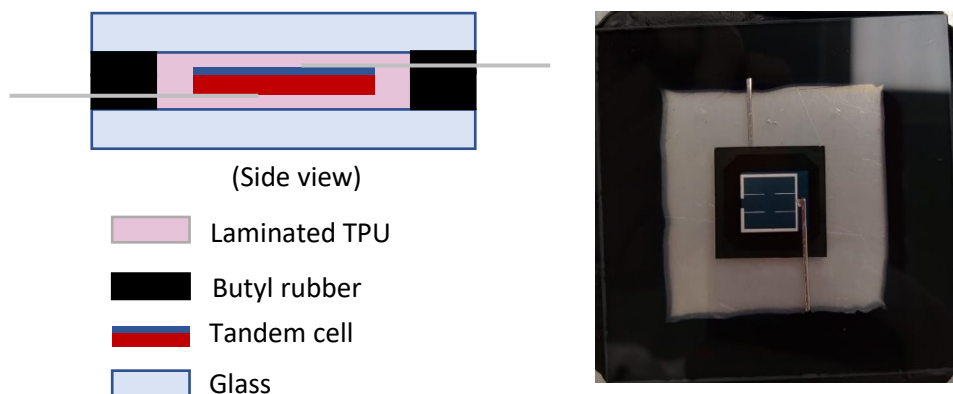

(Side view)

Laminated TPU

Butyl rubber

Tandem cell

Glass

Figure 2.3: *Mini-module side view schematic representation (left). Minimodule top view picture (right).*

present in the paste, a thermal annealing at 120°C under mild vacuum for 10 minutes has been carried out.

Measurement setup

Once the tandem devices were fabricated, their J-V characteristic curve was collected before and after encapsulation. To do this, a Wavelabs Sinus 220 LED based solar simulator with AM1.5G irradiance spectrum was used as light source, coupled it with a Kiethley 2400 series SourceMeter to take the J-V measurements in air. The data was recorded via a homemade MATLAB based software. The devices were measured from -0.1 V to +1.9 V in forward and reverse scan directions with 10mV of step-voltage, under dark and illumination conditions. The device's active area was defined with a laser-cut shadow mask, with an aperture of 1 cm^2. The light intensity was calibrated using a Fraunhofer ISE CalLab certified c-Si solar cells.

EQE measurements were collected using a LOANA system (PV-Tools). The chopped monochromatic light beam was focused entirely on the active area of the solar cell, avoiding the silver fingers. The light portion shining onto the silver finger is reflected, creating an artefact in the measure. Two bias lights were employed. The first one, a near-infrared LED (950 nm), allows to isolate the current response of the perovskite top cell, while biasing the silicon bottom cell, in addition, a 0.6 V bias voltage was applied. To measure the signal from the silicon top cell a blue LED light (525 nm) was used to saturate the perovskite top cell and the same 0.6V bias voltage was applied. Figure 2.4 shows the typical EQE signal given by the perovskite/silicon tandem solar cell. In red and in blue the absorption signals of the perovskite and the silicon subcells respectively, in grey the amount of light lost because of parasitic absorptions and above the 1-R curve the portion of the incoming light that is reflected.
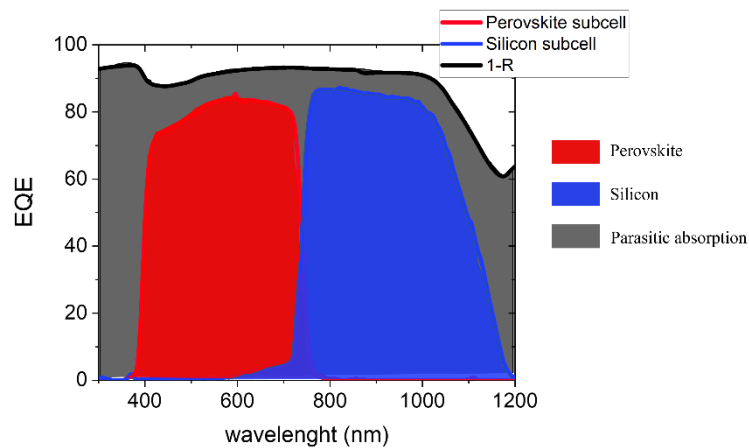

Figure 2.4: *Typical EQE absorption signal given by a perovskite/silicon tandem solar cell.*

As we will see later the different polymer materials adopted as encapsulants have been optical characterized. Absorption and reflection measurements were collected with the UV-Vis-NIR PerkinElmer Lambda950.

Angular dependency setup

The preliminary angular dependency behavior of perovskite/silicon tandem minimodule was studied by measuring the J-V characteristic curve for different values of the incident angle of the light. We defined as θ the angle of incidence (AoI), which is the angle between the incident light direction and the normal direction with respect to the minimodule's surface (a representation is shown in figure 2.5a). Therefore, when $\theta = 0°$ the angle between the incoming light and the cell's surface is 90°. The sample holder was custom made using a rotating clamp with a protractor. Once, the sample holder was ready we calibrated the angle, ensuring that when the minimodule's surface was parallel to the ground the angle on the protractor was zero. The J-V characteristic curve was measured with the same set up described in the previous paragraph, with the only difference that now the distance between the minimodule and the light source is smaller compared with the standard configuration. Thus, we calibrated the light intensity using the certified c-Si solar cell for multiple angles. The angles we selected for the experiments are 0°, 5°, 10°, 15°, 20°, 25°, 30°, 35°, 40°, 45°, 55°,65°, and 70. During the calibration, we waited a certain amount of time between the different measures in order to avoid possible effects on the performances given by the increasing of the sample's temperature (increasing the temperature increases the current output of a solar cell). Moreover, the sample rotation was done manually, as a result, the angle positioning is subjected to certain errors given by the operator. Hence, to evaluate this error the same measures were obtain in the back direction, thus from 70° to 0°.
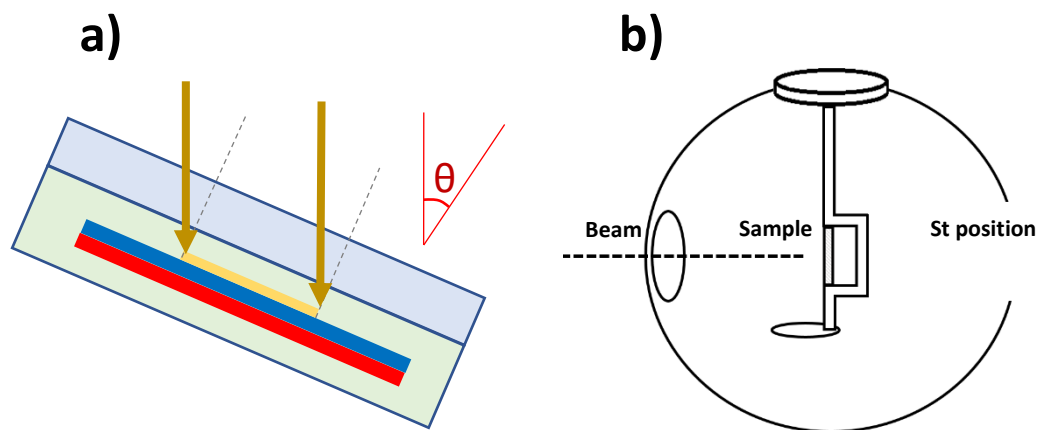

Figure 2.5: a) Representation of the minimodule tilted of a certain angle (in yellow the active area, in blue the perovskite top cell and in red the silicon bottom cell). b) Schematic representation of the sample holder utilized for the angular dependency reflection measures.

The angular dependency reflection measures were collected with the UV-Vis-NIR PerkinElmer Lambda950. In this case, a mount center sample holder has been used and placed inside the integrating sphere (figure 2.5b), and the signals were measured for 0°, 5°, 10°, 20°, 30°, 40°, 50°, 60°, 70°.

The angular dependency EQE measurements were collected with the Enlitech QE-R quantum efficiency system. The chopped monochromatic light beam was focused entirely on the active area of the solar cell, again avoiding the silver fingers. Also in this case two bias lights were employed. The first one, was a polychromatic lamp, in which a filter that cut all the wavelengths below 500nm was installed. With this filter, the silicon response was saturated and only the EQE signal coming from the perovskite subcell was collected. The same approach could be employed to measure the silicon subcell, hence using a filter that cut the wavelengths above 700nm, saturating the perovskite subcell and thus, collecting the EQE signal of the silicon subcell. Unfortunately, the bias light was not intense enough to saturate the perovskite subcell with the result of obtaining a certain percentage of EQE signal in the perovskite region, and a silicon peak intensity well below the real value. For this reason, a blue LED light (525 nm) was installed and turned on for the silicon signal collection. Even in this case, a -0.6V bias voltage was applied during the measure. Similarly to the other angular dependency measurements the EQE signal was collected for the following values of angle: 0°, 5°, 10°, 20°, 30°, 40°, 50°, 60°, and 70°.

As opposed to the Loana system mentioned before, in which there is a stage that, once calibrated, automatically adjusts the distance from the sample to the light source, in this case, the position was manually adjusted on beam focus position. A picture of the Enlitech set up is shown in figure 2.6.
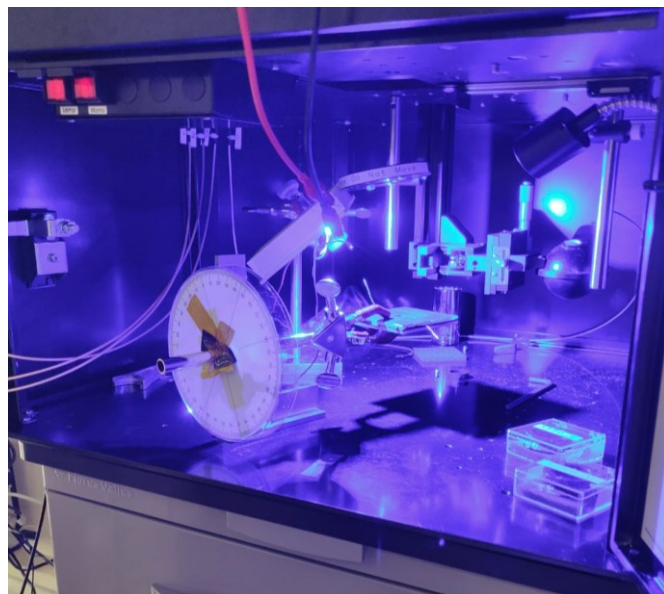

Figure2.6: Angular dependency EQE set up

Outdoor testing

Once the minimodules have been measured in the laboratory with the angular dependency setup, we took the devices to the New Energy Oasis (NEO – Kaust, Saudi Araba) test field to evaluate their efficiency under real conditions and compare them with the data collected in laboratory. To acquire photovoltaic data, we used a J-V tracer from EKO (model MP-160). The I-V characteristics of multiple samples were probed successively using the multiplexers MI-520 again from EKO. The J-V characterize curves were collected every 10 minutes with a scan rate of 200mV/s. The electronic equipment was kept inside a cooled house at 23°C and data acquisition was performed with a computer running EKO's MP160 software. The global horizontal irradiance on the plane of the devices was measured using the pyranometer MS-802 (EKO), which was mounted on the same structure as the devices. The solar minimodules were mounted with South orientation and on a structure with a tilt angle of 25°. The KAUST's testing field is located inside the KAUST campus, near the village of Thuwal (Saudi Arabia; 22.302494, 39.110737). Furthermore, solar spectra were acquired using the spectrometers QE65PRO (visible spectral region) and NIRQuest512 (NIR spectral region) from Ocean Optics. The spectrometers were built into a temperature-controlled housing and possess a wavelength resolution of < 2nm across the entire VIS/NIR.

Stability tests

With commercialization as final goal, one of the most important criteria thar has to be satisfied is the stability, which allow to guarantee a certain time of warranty for the product. Many articles concerning the stability of perovskite solar cells (PSc) have been published over the last few years.[36–38] The most recent and advanced of these studies explored the same conditions that are used to evaluate the accelerated degradation of silicon modules. These tests are part of the so-called IEC 61215 standard, fully entitled as the "terrestrial photovoltaic modules – design qualification and type approval".[39] The IEC 61215 is a series of very detailed, time consuming, and interconnected stress tests that provide accelerated aging conditions to evaluate the potential long-term lifetime of a solar module. The technologies in the market such as Si and GaAs passed the full IEC 6125. Therefore, perovskite must pass these tests too if they aim to challenge the same PV market. Anyhow, since perovskite/silicon tandems are going to share the same portion of market of c-Si technologies (either residential or utility) they must succeed in these tests. Furthermore, such tests may help to better understand the degradation mechanisms in PSc and thus allow to block or prevent them. These tests evaluate the stability of the system on a module level, thus, even if the cell is still working perfectly after the test, the module failure means that the utilized architecture is not suitable for commercialization. It is important to mention that the IEC 61215 is only a minimum requirement. To guarantee a 25 years lifetime, it is necessary to pass the IEC test multiple times. From figure 2.7 we can see the test sequences that characterize the IEC 61215 standard. Each sequence contains several stress tests that aim specifically for one of the identified main degradations causes that commonly occurs. In this work, the tandem solar minimodule will be subjected to two tests, the damp heat test in which the sample is exposed to 85 ± 2 °C at a relative humidity (RH) of $85 \pm 5\%$ for 1000 hours, and 50 cycles of thermal cycling where the temperature varies between -40 ± 2 °C and 85 ± 2 °C. The temperature needs to stay stable at least for ten minutes and temperature ramp has to be maximum 100°C/h. The first one aim to study the isolation of the minimodule configuration and the stability with the temperature, while the second one allows to evaluate possible delamination of the encapsulant. A more detailed discussion is presented in the result and discussion chapter.
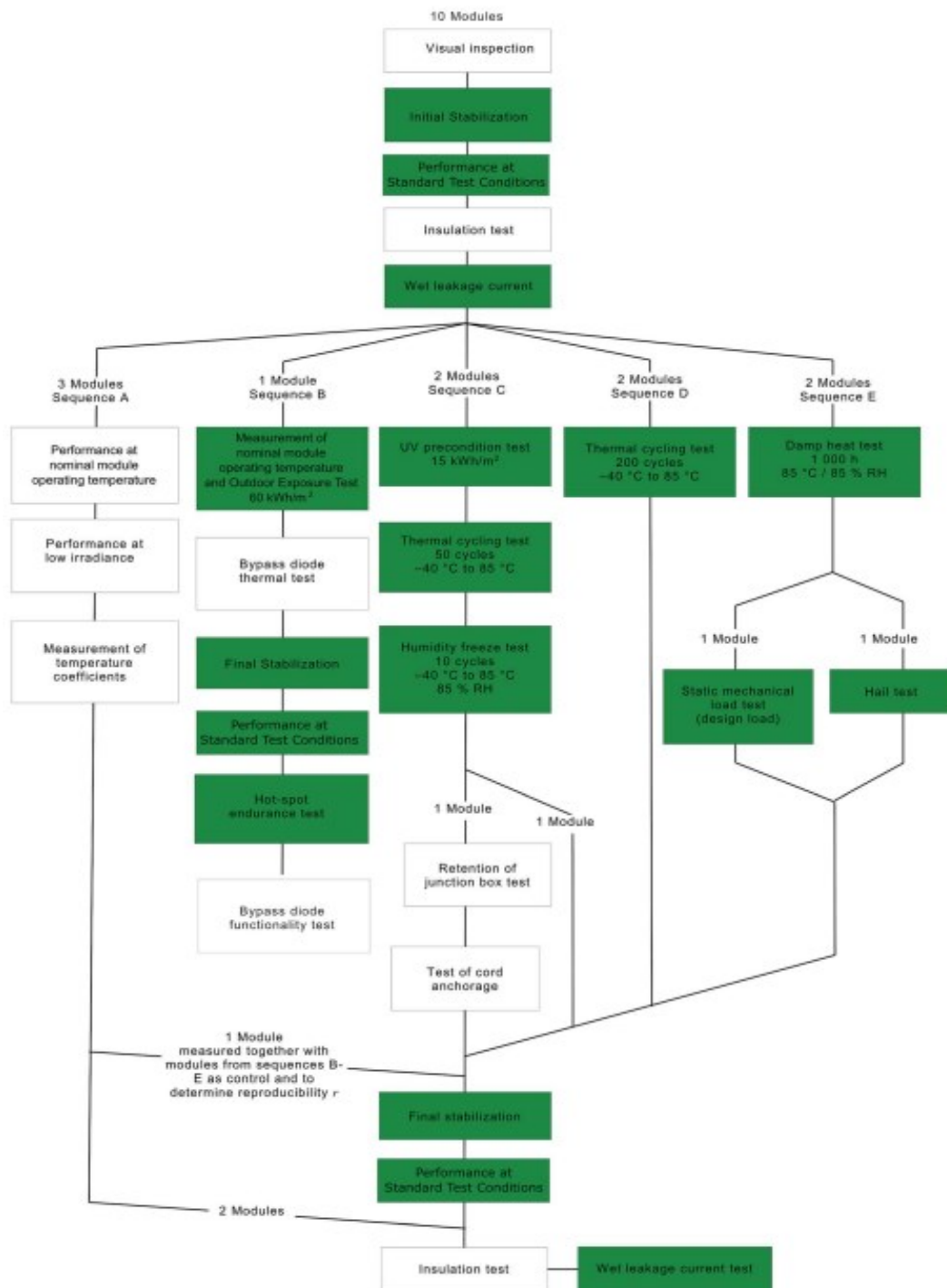
Figure 2.7*: Full test flow for design qualification and type approval of PV modules.*[39]

Chapter 3

Results and discussion

This chapter is divided into two parts. The first part addresses the challenges to improve the stability of perovskite photovoltaics, in particular perovskite/silicon tandems. Therefore, here are described the encapsulation strategies to protect the solar cells from the environmental degradation. Contrarily to silicon technologies, perovskite photovoltaics are quite sensitive to processing conditions, temperature in particular cannot exceed 140 °C. This strongly limits the choice of processes and materials available for the encapsulation. In the first part, we thoroughly describe the encapsulation process using thermoplastic polymers that are of relevant interest for the industrial field. The second part addresses the angular dependency performance of perovskite/silicon tandem minimodules. Indeed, in real applications, solar cells are exposed not only to different light intensities, but also to different irradiation angles. In lab experiments, these conditions are never considered. For the first time, we recreated in the lab the variation of the performances of the tandem, mimicking the different irradiation conditions that a solar cell experiences outdoor. Moreover, since the current output of the tandem is strongly linked to the current matching condition between the two subcells, we thoroughly investigated the current response at different angles for both the perovskite and the silicon subcells. Our findings will help to improve the understanding of the potential of the tandem technology looking at real applications.

Efficient and reliable encapsulation of perovskite/silicon modules

Solar cells need to be integrated into solar modules in order to be exploited to generate electricity. Industrially, the fabrication of perovskite/silicon tandem modules resemble the fabrication of c-Si modules. This process includes the tabbing of the cells into strings, the lamination of the strings between the front and rear glasses, and the application of the junction boxes. However, so far, only Oxford PV reported the successful fabrication of industrially sized perovskite silicon tandem modules.[40] Contrarily, most of the academic research is developed on "mini-modules" that include only one cell (usually with an active area of 1 cm^2). This allows for multiple experiments and a lower bill of materials. In these mini modules, the terminals of the tandem are secured with two ribbons (see the method chapter for more details). The cell is placed between two glasses, which act as protective
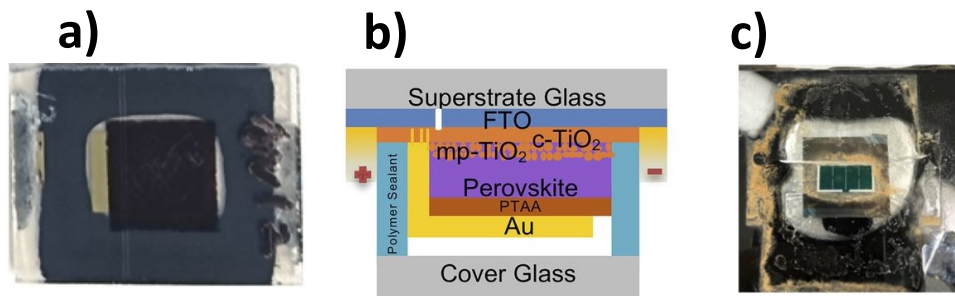
Figure 3. 1: a) Device encapsulated with PIB picture and b) schematic representation.[41] *c) Picture of the device with the inner atmosphere saturated with perovskite byproducts.*[42]

barriers, and sealed. The sealing process is not trivial. Indeed, perovskites are sensitive to high temperature processing (>140 °C), which causes the sublimation of the small volatile organic cations (typically methylammonium or formamidinium). Therefore, the first attempts to fabricate minimodules used poly isobutylene (PIB, butyl rubber) on the edges of the glass as a sealant. PIB had the advantage of a low temperature processing (<100 °C), hence compatible with the perovskite's constraints. With this encapsulation, (figure 3.1 a and b) Shi et al. reported for the first time the passing of three IEC stability tests for perovskite single junction solar cells: the damp heat, the thermal cycle, and the humidity freeze.[41] However, the performances of the devices were quite low, and not representative of the perovskite potential. A major weakness of the PIB sealing was the formation of an atmosphere of perovskite byproducts within the glasses packaging. This atmosphere, mostly composed by iodomethane, was interacting with the metal electrodes, degrading them. Similarly, De Bastiani et al. used PIB encapsulation to protect perovskite/silicon tandems in a six-months outdoor experiment. Even in this case, the authors found that the inner atmosphere saturated with perovskite byproducts corroded the silver electrodes, failing the performances (figure 3.1c).[42] More recently, Azmi et al. reported the first perovskite single junction solar cell that passed the IEC damp heat test with a final efficiency >20%, making it competitive with the best of the silicon technologies (figure 3.2).[43] The main progress of Azmi et al. was the inclusion of a thermoplastic polyurethane encapsulant together with the PIB sealing of the edges. With the encapsulant, the degradation was significantly minimized, opening a new chapter for the stability of
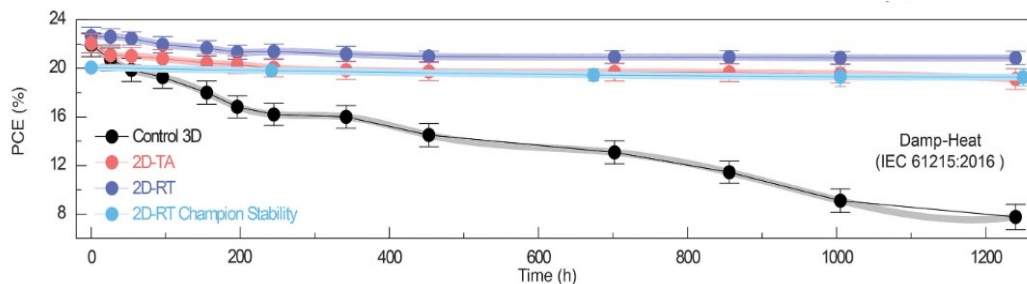

Figure 3.2: Damp heat test for different PScs configurations. With control 3D the author refers to the unencapsulated device.[43]

perovskite photovoltaics. Ethylene-vinyl acetate (EVA) is the most common encapsulant for solar modules. It owes its fame to good barrier properties and remarkable transparency at an affordable price. It is a thermosetting polymer, with a cross-link temperature of 140-150 °C. Usually, it is vacuum laminated at the front and rear of the silicon strings of cells, to seal the front glass with the rear polymeric back-sheet. Rarely it is used in glass/glass configuration. Indeed, during the cross-linking process, the byproducts of the reaction are expelled from the polymeric back-sheet, while they would be trapped in the case of double glasses. Unfortunately, EVA is not suitable for the encapsulation of perovskite photovoltaics. Firstly, the lamination temperature is too high. Secondly, perovskite photovoltaics require a mandatory glass/glass encapsulation. This because the conventional polymeric back-sheets are not a strong enough barrier against moisture permeation, which is one of the major degrading agents for the perovskite. Thirdly, the rigidity of the cross-linked EVA makes it prone to induce delamination in the perovskite cell (figure 3.3). Perovskite devices, either in tandem or single cell configuration, include in their architecture several materials (compact oxides, organic, nanoparticles, etc.) with diverse expansion coefficients. For this reason, the mechanical reliability of perovskite photovoltaics is quite an issue and requires a dedicated effort to be solved. Without the option of using EVA, there is currently an open challenge to find the right material candidate to set the first generation of efficient and stable perovskite-based solar modules. In the next paragraphs, we explore two promising families of encapsulants that are currently under consideration to fulfill this role: the thermoplastic polyurethanes and the poly olefins.

Figure 3.3: Initial delamination induced by EVA.

The lamination processes

The lamination is the process of manufacturing materials with multiple layers so that the final composite product has better properties than its single components. In photovoltaic jargon, the lamination defines the process of sealing a solar module. The lamination can be performed in vacuum or in air. Vacuum lamination is the most common practice in the photovoltaic industry. Here, the modules are arranged and aligned in the "lay-up" phase, where the strings of cells are positioned between two layers of encapsulants and sandwiched between the front glass and the rear back-sheet. It is important that there are no imperfections or dust particles in between the encapsulant sheets to guarantee a proper sealing. The vacuum laminator is composed of two heating plates (top plate and bottom

plate), a rough vacuum pump, a top membrane for pressure control, and two Teflon sheets to protect the plates from the excess of encapsulants. Initially, the vacuum laminator applies a rough vacuum (1×10^{-1} to 1×10^{-3} mbar, depending on the system) that sucks out the moisture trapped in the materials. Subsequently, the top membrane starts inflating. This increases the pressure on the top side of the module, pressing it against the bottom. Finally, the vacuum is removed, and the sealed module is extracted from the laminator. The parameters that govern the lamination are the temperature of the plates, the processing time, and the pressure used. Usually, there are multiple steps of vacuum and pressure to achieve optimal lamination, making the process strongly dependent on the know-how of the operator. Non-optimal lamination can present clear signs of defects (such as bubbles and non-laminated areas) or leaks and small percolation paths that are harder to identify with standard quality control. Alternatively to vacuum lamination, the lamination in air is usually used for roll-to-roll processes. However, this approach is not suitable for perovskite photovoltaics, unless secured in a nitrogen environment, and therefore not discussed further. The following figure shows a typical vacuum lamination profile of a solar module, reporting the pressure between the two plates versus time at a fixed temperature.
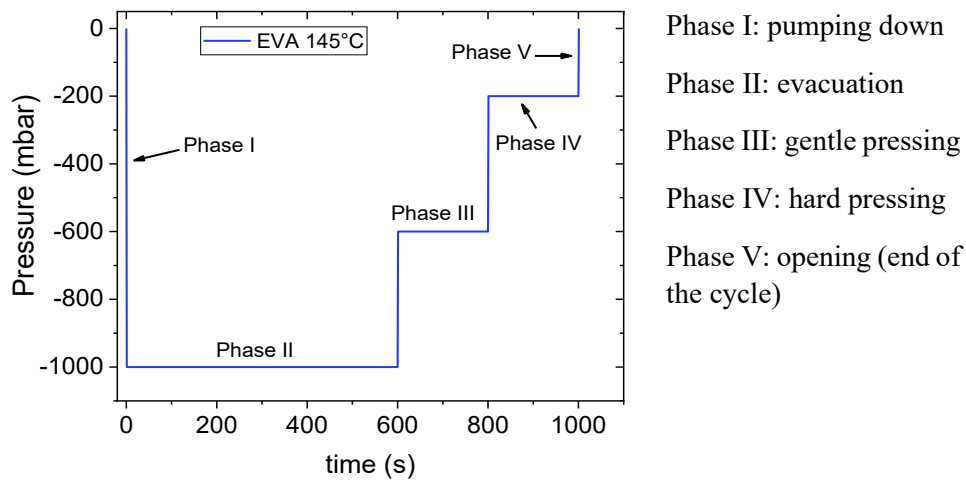

Phase I: pumping down

Phase II: evacuation

Phase III: gentle pressing

Phase IV: hard pressing

Phase V: opening (end of the cycle)

Figure 3.4: Employed pressure profile for the encapsulation with EVA as encapsulant.

Improving the optics of perovskite/silicon modules

The performance of a solar module depends on the performances of the cells used minus several losses that occur in the transition from cell-to-module. These losses can be due to the design of the module, the size and the geometry of the wafers, and the space taken for the tabbing. The geometrical fill factor (to not be confused with the solar cell fill factor) takes into account all these factors, summarizing in one percentage the non PV-active fraction of the module. Interconnecting the cells into string adds series resistance proportional to the length of the ribbons and the quality of the soldering. Both reduce the
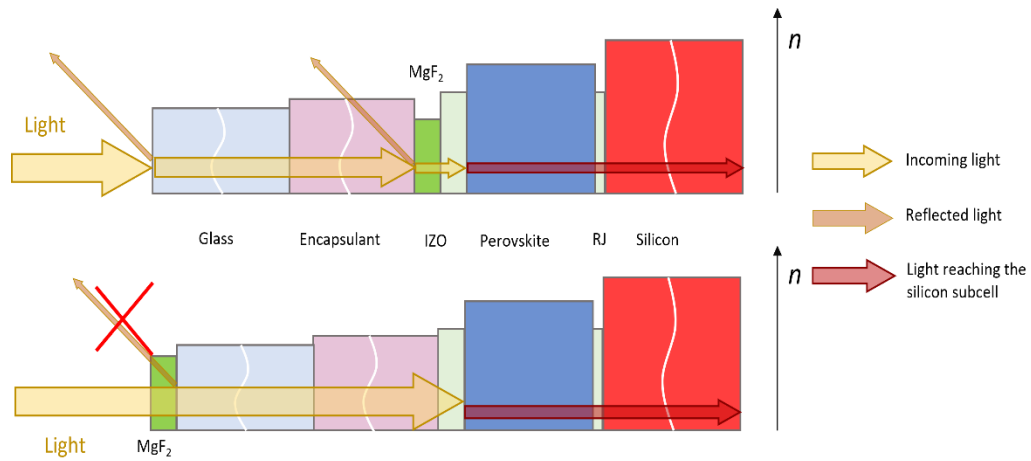
Figure 3.5: Representation of the refractive indexes of the different materials involved in the tandem device.

performances of the module analogously to the effect of high series resistance in solar cells. Lastly, the front glass used to seal the module and the encapsulant induce optical losses. Indeed, the glass brings a reflection loss at the front surface (usually around 4% loss) while the encapsulants generate optical parasitic losses in the UV and near-IR regions, reducing the EQE of the module. Moreover, at the research level, most of the cells are not meant to be fabricated looking at module integration. For this reason, the lab cells often implement anti-reflective coatings (ARC) at the sun side that are not compatible with the module configuration. A clear example that we faced in this study is the presence of MgF$_2$. In
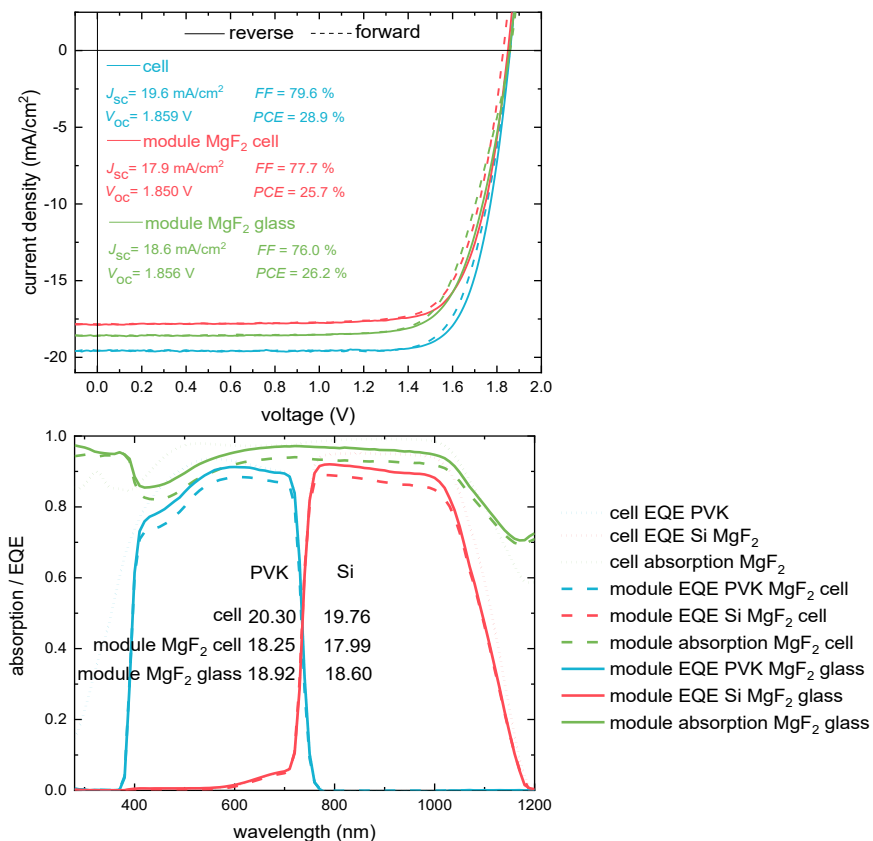

Figure 3.6: Characteristic JV curves (top) and EQE measurements (bottom) of the unencapsulated device and the two module configurations.[46]
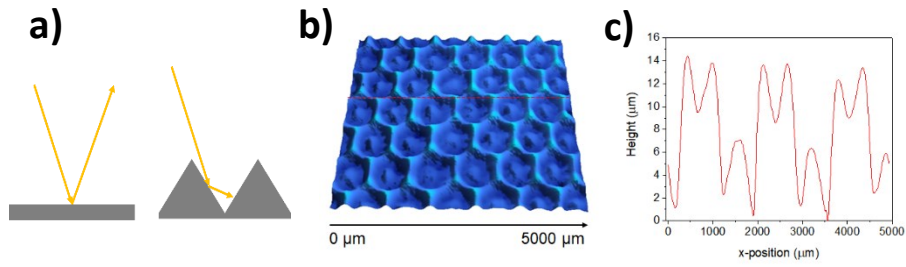
perovskite/silicon tandems, MgF_2 (alternatively LiF) is always deposited with a thickness between 90-140 nm on the IZO transparent electrode facing the sunlight. The MgF_2 reduces the reflection losses due to a better in-coupling of the light, thanks to its refractive index that well matches with air. It is also used to favor the current matching condition, for example minimizing the reflection losses either in the perovskite or the silicon sub-cells, respectively. Therefore, MgF_2 covers a very important role in the device optics. However, once these tandems are laminated in minimodules, the MgF_2 is not facing air anymore, but the encapsulant and the glass, whose refracting indexes are higher than MgF_2. In turns, this creates a refractive index mismatch that induces a new reflection rather than suppressing it. Figure 3.5 plots the refractive indexes of the different materials involved in the tandem device with an approximation of the thickness. Therefore, we started our investigation comparing minimodules of perovskites/silicon tandems laminated with MgF_2 on top of the IZO top electrode and on top of the outer front glass. Figure 3.6 shows the representative JV of the two minimodules and the unencapsulated cell (with the ARC on top of the IZO). It is clear that the device with MgF_2 has a lower current, which is due to higher reflection losses as shown by the absorption curve in the EQE plot (figure 3.6). Moreover, it has been observed that the MgF_2 reduces the resiliency of the minimodules, making them more prone to the phenomenon of delamination.[44] Obviously, in industrial applications, MgF_2 will not be included in the tandem device, but will rather be used as ARC on top of the front glass. Indeed, the ARC layer can be used to mitigate the 4% reflection loss caused by the front
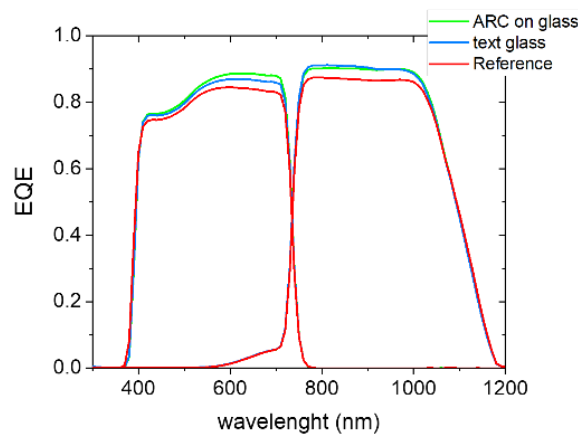
glass. Similarly to MgF$_2$, another strategy is to use textured glasses. This approach is well-known in the silicon industry, where silicon wafers are textured to obtain randomly distributed pyramids that reduce the reflection of the incoming light with multiple absorptions. Figure 3.7a shows a sketch of the texturing effect and the reduction of the reflection of a silicon wafer. Unfortunately, the amorphous nature of glass does not allow for a precise texturing, like in crystalline silicon, but requires several etching steps with polymeric masks. The texturing can be on one side or on both sides. In our case, we opted for a single side textured glass. To map the morphology of the texturing, we collected the 3D-profile of the glass surface (figure 3.7b and c). The texturing is defined by a honeycomb structure, with micrometer-high features. To improve the optics of our perovskite/silicon tandem minimodules, we compared the performances of three modules: one laminated with flat glass as a reference, one with MgF$_2$ ARC, and one module with textured front glass. Figure 3.8 shows the EQEs signals. It is clear that the reduction of the reflection increases the current for the MgF$_2$ and the textured modules. Controlling the optics of the module is of paramount importance to achieve high performance. Indeed, here we have shown with two relatively simple implementations (removing the internal reflection due to the MgF$_2$ layer on the top of the tandem and reducing the front glass reflection) that the current output can be significantly enhanced, resulting in an absolute gain in current density of 3.8%. In the next two paragraphs, we will explore the role of the encapsulants on the module performances.

The thermoplastic polyurethane encapsulant

The encapsulants are the polymers that seal the module. Conventionally EVA is the reference encapsulant for the silicon industry, but we have demonstrated that it is not suitable for the lamination of perovskite- photovoltaics. Thermoplastic polyurethane (TPU) is a promising candidate to replace EVA. TPU does not cross-link, therefore it can be processed at lower temperatures than EVA. Figures 3.9a, b show the lamination process module sealing with TPU together with the actual temperature reached by the solar cell during the process (we measured the temperature of the tandem laminating a thermocouple on the rear of the device, within the two glasses, figure 3.9c). We also measured the TGA of TPU and we did not observe any sign of chemical reaction (figure 3.9d). TPU has a high transparency in the range between 380-1200 nm, with a significant absorption below <380 nm (figure 3.9e). In this way, TPU covers the double role of encapsulant and UV-barrier. However, the UV absorption must be taken into account when designing the tandem configuration, since it will affect the current output of the perovskite top cell. Figure 3.9f shows the EQE of a perovskite/silicon tandem before and after the encapsulation, with the clear cut-off edge of the TPU. One challenge that we faced when encapsulating perovskite/silicon tandems is the delamination of the perovskite top contact. It has been reported that the adhesion between the C_{60} ETL and the SnO_x buffer layer is weak and prone to separation when exposed to mechanical stress.[44] We experienced two types of delamination: macroscopic and microscopic delamination. Macroscopic delamination is visible by eye and clearly shows the lifting of the encapsulant from the cell (see figure
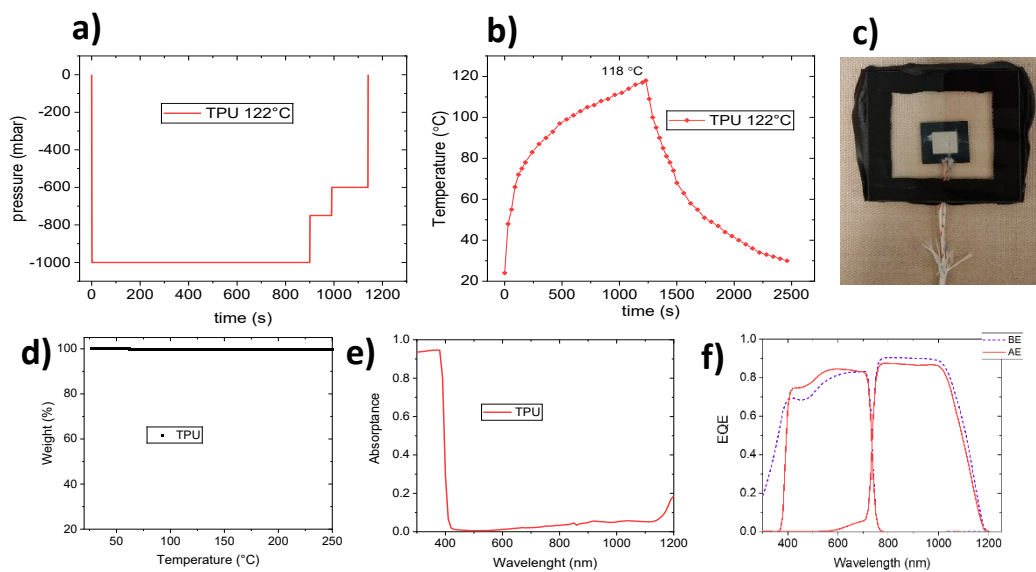

Figure 3.9: Pressure a) and temperature b) profiles for the encapsulation process with TPU as encapsulant. c) Picture of the thermocouple inside the minimodule. d) TGA profile of TPU. e) UV-Vis absorption spectrum of TPU. f) EQE measurements before (dotted line) and after (full line) encapsulation with TPU.
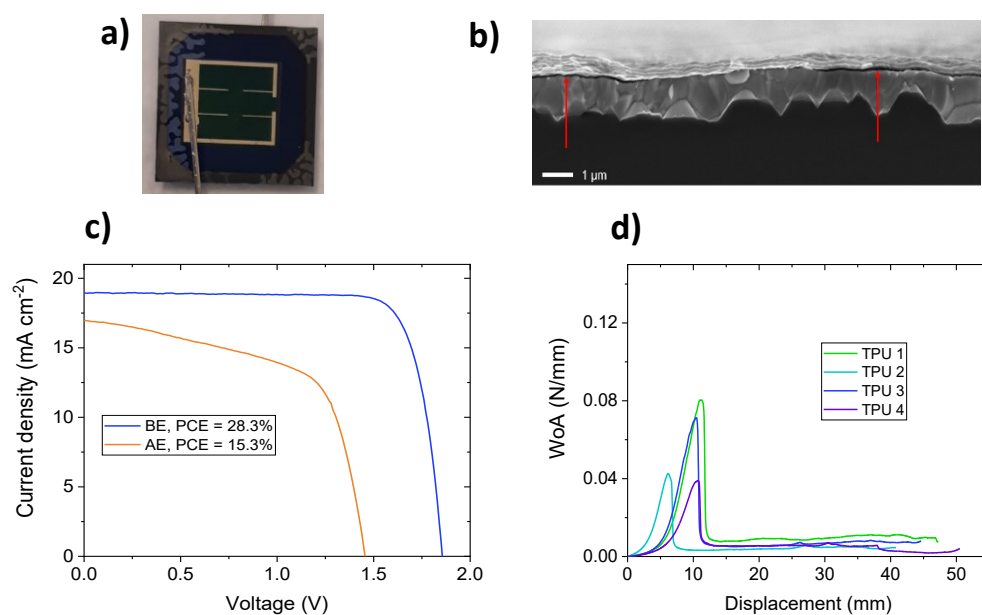
Figure 3.10: a) Macroscopic and b) microscopic delamination of front side of the device. c) JV curves before and after encapsulation in which there is a loss in the performances after encapsulation. d) delamination measures with TPU.

3.10a) causing the catastrophic failure of the device. The microscopic delamination is localized to micrometer areas and visible via Scanning Electron Microscopy in cross-section (figure 3.10b). Here, the losses in performances are reduced, leading into a reduction of the Voc, FF and Jsc (figure 3.10c). To better understand the delamination mechanism, we performed adhesion experiments after the lamination of the TPU on the tandem cell. In the adhesion experiments, we evaluate the work of adhesion of the weakest interface. Figure 3.10d shows the work of adhesion profiles for four identical samples. After an initial tensioning of the TPU we see an abrupt drop in the adhesion, which overlaps with the beginning of the delamination. The adhesion values that we obtained matches with those reported in the literature, confirming that the weakest interface is that between the C_{60} ETL and the SnO_x buffer layer. To minimize the effects of the delamination, we thoroughly optimized the lamination process, controlling the amount of pressure applied and the duration of the process. Next, we fabricated perovskite/silicon tandems that we encapsulated in minimodules using TPU and two glasses. The JV curve of the champion device is reported in Figure 3.11a. Prior to the delamination the device shows a Jsc of 18.6 mA/cm^2, a Voc of 1851 mV, a FF of 78.8%, resulting in a PCE of 27.1%. After the lamination, the figures of merit are almost preserved; the laminated device shows a Jsc of 17.9 mA/cm^2, a Voc of 1844 mV, a FF of 79.1% and a final PCE of 26.1%. The champion minimodule lost only an absolute 1% after the encapsulation, mostly due to a reduction in the current, proving the great success of the TPU and our encapsulation process. After the encapsulation, the EQE (figure 3.9f) shows the typical TPU cut-off at 380 nm, concomitant
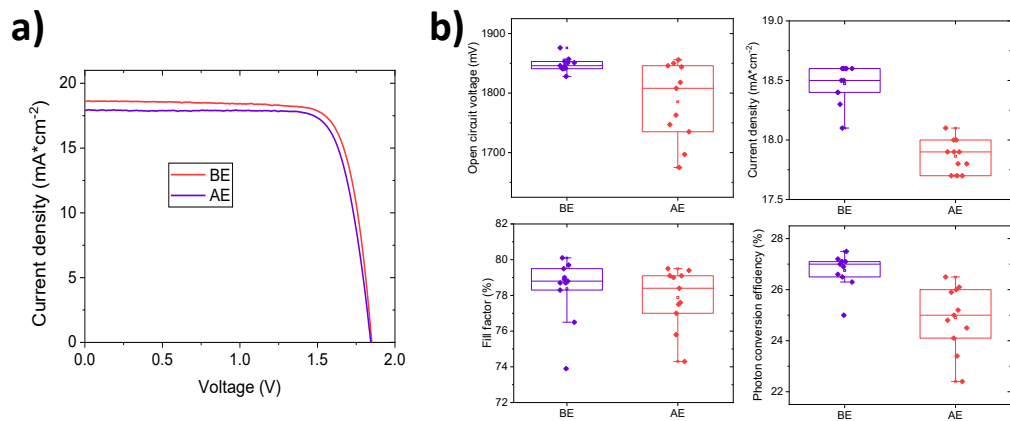
Figure 3.11*: a) JV characteristic curves of the champion device before and after encapsulation. b)Distribution of the figures of merit for the encapsulated batch of tandem.*

with an enhancement of the current in the perovskite region. This enhancement is due to a reduction of the reflection losses due to a better in-coupling of the light, since the TPU acts as weak ARC. However, the presence of the front glass added extra reflection losses that caused the overall reduction of the current and, hence, the PCE. To validate our process, we reported the statistical distribution of the encapsulation of a whole batch of tandems. Figure 3.11b shows the distribution of the figures of merit for the encapsulated batch of tandem. The main loss is due to a reduction in the current, which we expected from the EQE measurement.

The polyolefin encapsulant

Another promising class of encapsulants are the polyolefins (POE). Compared to the TPU, which is not popular in the photovoltaic industry, the POE is widely used in the lamination of flexible silicon modules. Nowadays, there are many different types of POE commercially available, therefore it is quite difficult to determine the exact composition of the polymers involved. In our experiments, we used a POE from Borealis. Similarly to the TPU, also Borealis is a thermoplastic material. Indeed, the TGA does not show any sign of chemical reaction in the temperature range used for the lamination (Figure 3.12a). In figures 3.12b and c we report the lamination temperature and pressure profiles of the encapsulation process with POE. Compared with TPU we used a lower lamination temperature, which might be beneficial for the final performances, but on the other hand to ensure a good lamination and avoid bubbles the encapsulation time must be longer. Optically, the POE is more transparent than the TPU in the UV region (figure 3.12d) but has higher parasitic absorption in the near-IR, concomitant with the absorption of the silicon sub-cell. Indeed, the EQE of a laminated tandem (figure 3.12e) shows a higher current response of the perovskite at the expense of a current reduction in the silicon sub-cell. Once more, this emphasizes the importance of the module design on the right choice of the perovskite bandgap looking at the current matching condition. Respect to the TPU, Borealis is more prone to delamination. Indeed, we noticed a higher rate of failure when encapsulating the tandems. Most of the delamination was happening during the cooling of
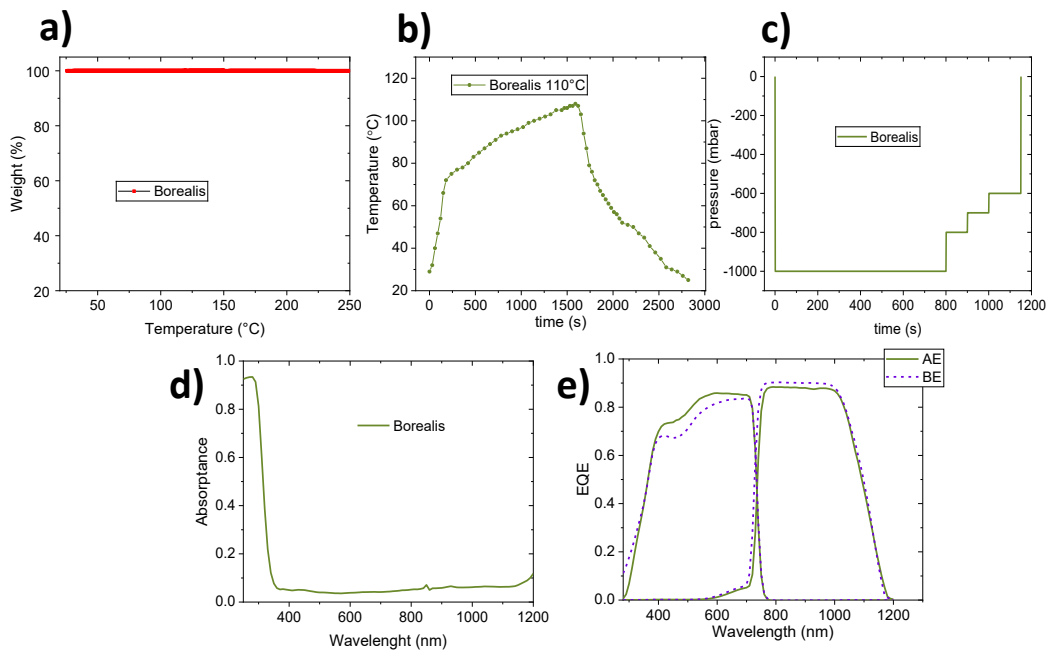

Figure 3.12*: a) TGA profile of Borealis. b) Temperature and b) pressure profile of the encapsulation process with Borealis as encapsulant. d) UV-Vis absorption spectrum of Borealis. d) EQE measurements before and after encapsulation with Borealis.*
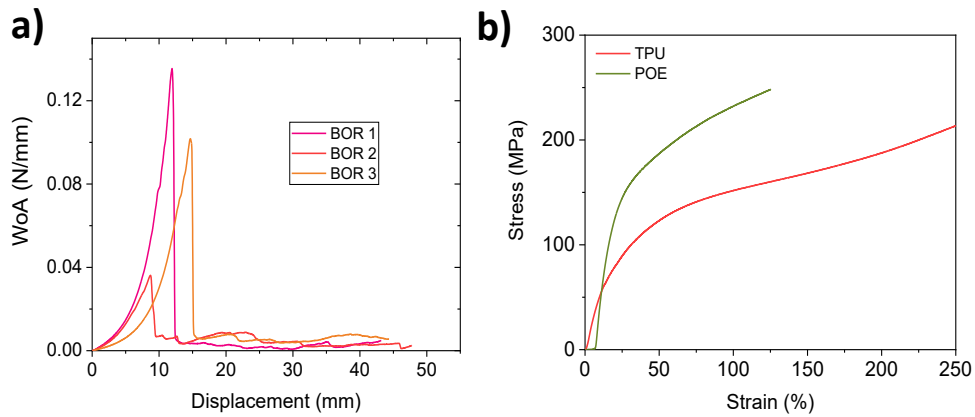
Figure 3.13: a) Delamination measures with Borealis. b) Stress-strain curves for TPU (red) and Borealis (green)

the samples, straight after we removed them from the laminator. To better understand the origin of this mechanism, we evaluated the work of adhesion of the samples laminated with Borealis (figure 3.13a). Compared with the TPU, the profiles achieve on average higher adhesion values before the failure, which should suggest a better resilience against the delamination. However, we also measured the tensile stress test to evaluate the Young modulus (figure 3.13b) and we found that Borealis is more rigid than the TPU, hence transferring the stress caused by the thermal expansion coefficients directly to the weakest interface. Next, we encapsulated a batch of tandem devices to investigate the performances of the minimodules. Figure 3.14a shows the JV curve of the champion device before and after the lamination. The device before the encapsulation shows a Jsc of 17.8 mA/cm^2, a Voc of 1836 mV, a FF of 76.6%, resulting in a PCE of 25.1%. After the lamination, the minimodule shows a Jsc of 18.0 mA/cm2, a Voc of 1810 mV, a FF of 74.9% and a final PCE of 24.4%. Overall, the loss in performances is <1%. Importantly, the Jsc does not reduce like in the minimodule laminated with TPU. This reflects the higher transparency of Borealis, particularly in the UV region. Moreover, the EQE of the tandem before and
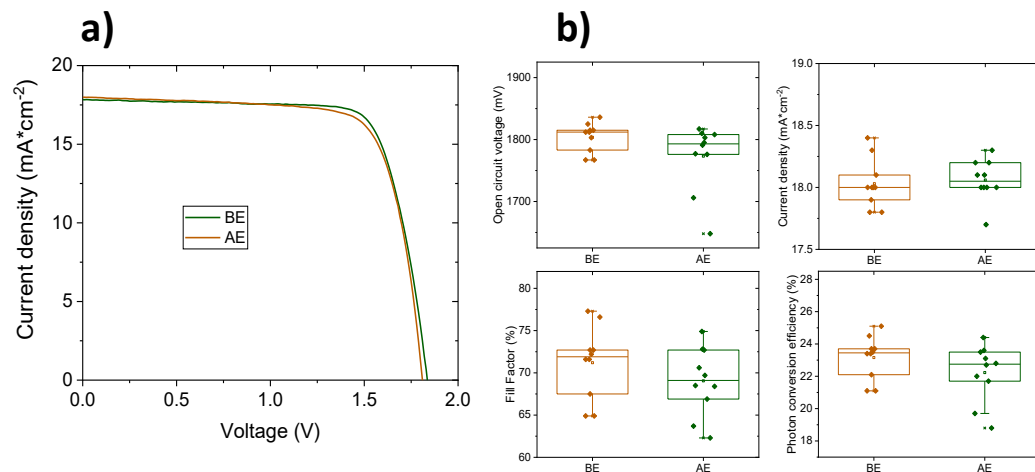

Figure 3.14: a) JV characteristic curves of the champion device before and after encapsulation with Borealis. b) Distribution of the figures of merit for the encapsulated batch of tandems.

after encapsulation shows the better in-coupling of the light, particularly in the perovskite sub-cell, which contributes to fight back the reflection losses induced by the front glass. To validate our findings, we performed a statistical analysis encapsulating a whole batch of tandems (figure 3.14b). Outstandingly, the tandems preserved their initial performances. In particular, the Jsc is slightly increased over the distribution of samples, testifying once more the excellent optical properties of Borealis.

Comparison between encapsulants and stability tests

In this study, we investigated the impact of the encapsulation process on perovskite/silicon tandems using two different encapsulants: TPU and Borealis. The TPU shines for its forgiveness in the lamination process, while Borealis is more prone to induce delamination of the tandem's top contact. However, the TPU has a strong absorption in the UV, which affects the performances and the current output of the tandem (therefore it requires a

	Voc (mV)	Jsc (mA/cm^	FF (%)	PCE (%)
B DH	1817	18.3	70.6	23.5
A DH	1822	18.1	68.9	22.7

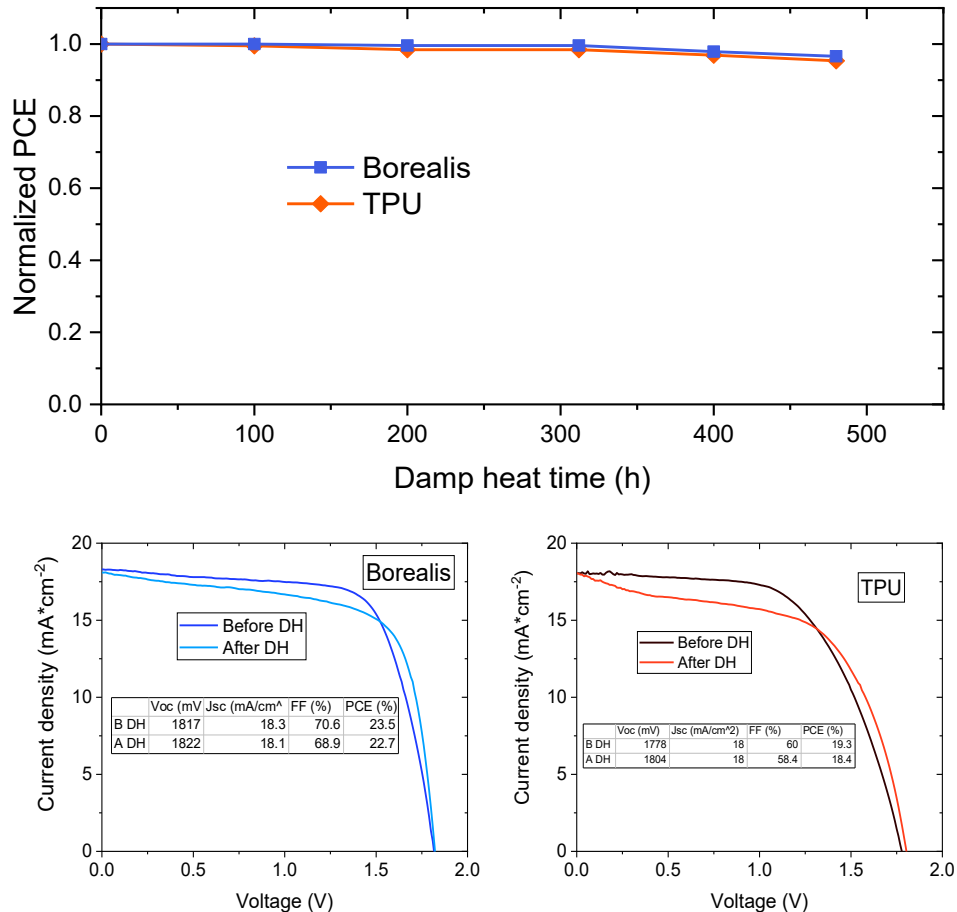|	Voc (mV)	Jsc (mA/cm^2)	FF (%)	PCE (%)
B DH	1778	18	60	19.3
A DH	1804	18	58.4	18.4

Figure 3.15: Preliminary damp heat test (top) and JV curves before and after 500 hours of test (bottom).

revision of the perovskite bandgap). Contrarily, Borealis is not reducing the current output but offers an exceptional anti-reflecting propriety that minimizes even the reflection losses of the glass.

Lastly, we undergo our minimodules laminated with TPU and Borealis to the harsh accelerated stability experiments. Improving the stability of the perovskite photovoltaics is of paramount importance for the commercialization of the technology. While many efforts have been placed to improve the stability of the single device (tandem or single junction), ultimately, it is the module that has to prove its stable performance. Since the perovskite/silicon tandem shares the same field of application of c-Si solar cells, the stability protocols must be the same. These protocols are under the international testing category IEC6125 and are composed of multiple experiments (see chapter 2). Here, we tested our minimodules according to the half damp heat test (85 °C, 85% relative humidity for 500 h) and the thermal cycle test (from -40°C to 85°C for 50 cycles). Figure 3.15 (top) summarizes the results of the damp heat test. Over 10 tandems minimodules laminated with TPU 8 failed the test, while over 10 tandems minimodules laminated with Borealis 9 failed the test. To fail the test, the normalized PCE must drop below 80% (T80). For those that passed the test, the performances are almost preserved. However, the TPU suffered a more severe degradation of the current, as shown in the JV curves before and after the test (figure

Borealis

	Voc (mV)	Jsc (mA/cm^2)	FF (%)	PCE (%)
B TC	1818	18.2	71.8	23.8
A TC	1819	18.5	72.5	24.3

TPU

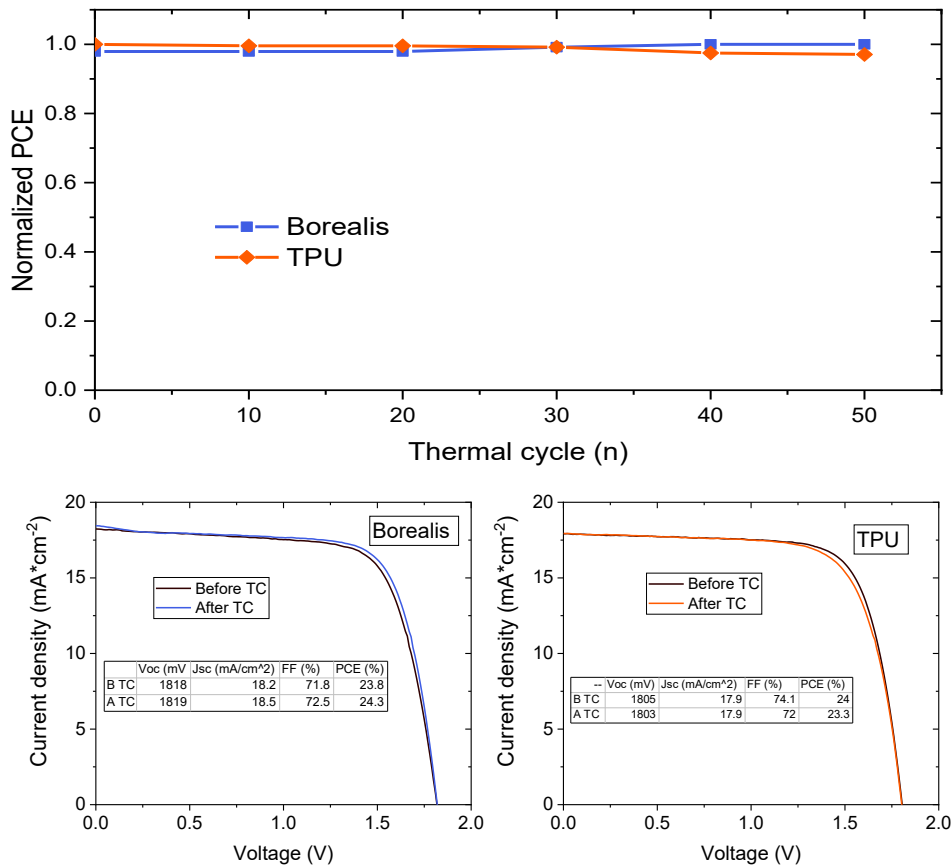| --	Voc (mV)	Jsc (mA/cm^2)	FF (%)	PCE (%)
B TC	1805	17.9	74.1	24
A TC	1803	17.9	72	23.3

Figure 3.16: Thermal cycling test results (top) and JV curves before and after the test (bottom).

3.15 bottom). On the contrary Borealis seems to better preserve the initial performances with minimal losses in the FF.

Figure 3.16 (top) summarizes the results of the thermal cycles experiment. Similar to the damp heat experiment, here 5 minimodules laminated with TPU and 5 minimodules laminated with POE were tested. Of these, 3 TPU minimodules and 4 Borealis minimodules passed the test (preserving a normalized PCE >80%). For both encapsulants, the losses are negligible as shown in the JV curves (figure 3.16 bottom). Contrarily to thermosetting polymers, the plastic nature of these encapsulants positively responded to the temperature cycles, with remarkable stability.

In conclusion the following table summarizes the pros and cons of the TPU and Borealis.

	Processing temperature	Processing time	Mechanical reliability	Optical properties	Commercially available
Thermoplastic polyurethane TPU	122°C	1150s	Good	Strong absorption <380 nm	yes - Swmintl
Polyolefin Borealis	110°C	1500s	high risks of delamination	Excellent transparency	yes - Borealis

Angular-dependent performances of perovskite/silicon tandem in experimental and outdoor conditions

As we already mentioned, throughout the day, solar cells are exposed to different light intensities and different irradiation angles. In a real application, the most important aspect that has to be considered is the energy delivered by the module during the day, i.e. the power (expressed in Wh Watts per hour). Therefore, commercial solar modules aim at the best power output during the day and the year, and the lowest possible cost. For this reason, it is crucial to understand the behavior of solar cells under real world conditions, in order to establish proper energy yield calculations that validate the potential of the technology in a shortcoming entrance in the PV market. Despite the great progress of perovskite/silicon tandems, very little has been explored regarding outdoor performances. This is because of the lack of stability (outdoor measurements last for days), lack of technology (in particular for the encapsulation) and lack of significant dimension (most of the lab-scaled devices have an active area <1 cm^2). In this work, we have developed a resilient encapsulation

strategy that allows our device to be stable for days. Therefore, we now shift our attention to the understanding of the tandem performances in real operando conditions. Firstly, for the first time, we reproduced in the lab the different irradiation conditions in terms of incident angles experienced by a solar cell during the day. Then, we compared our lab results with those collected in the outdoor testing field. We discovered that the condition of current matching between the two sub-cells changes during the day, hence changing the overall current output (and therefore power) of the tandem. We rationalized this variation thanks to our angular dependent characterization that showed a different current generation in the sub-cells at high incident angles. This effect is accentuated by the architecture of the device, in particular by those layers that have strong impact on the optical properties, such as the ARC.

Angular-dependant JV

Solar cells are characterized in the lab (and in the industry) under specific standards of light intensity. However, once installed outdoors, the light condition can change significantly. In particular its incidence, which is always perpendicular to the cell surface in lab tests, raises significantly the reflection losses. To investigate these losses, we developed a holder that can rotate, changing the incident angle of the light on the surface of the cell. We noted that increasing the angle of incidence (AoI), the solar cell performances change, and the major effect is observed in the current density. Considering an active area of 1cm^2 when the incoming light is not perpendicular to the module surface, the projected area reduces leading to a decrease in the Jsc. Without considering spectral changes, the current density during the day varies because of two major effects, the first one is the scaling of the effective area exposed to sunlight and the second one is attributed to reflection. Compared to the reflection losses, the area scaling effect gives the most important contribution to the Jsc loss, and its behavior can be expressed with cosθ, where θ is the incident angle of the light (with θ equal to 0° the cell is perpendicular to the incident light).[45] For the
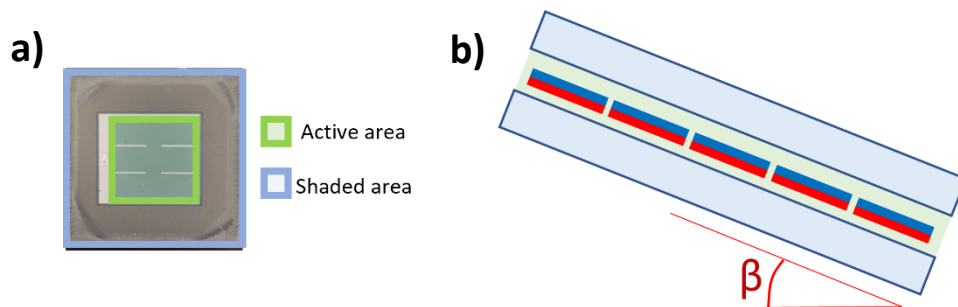

Figure 3.17: a) In light blue the portion of area shaded by the mask. b) Schematic representation of a solar module.
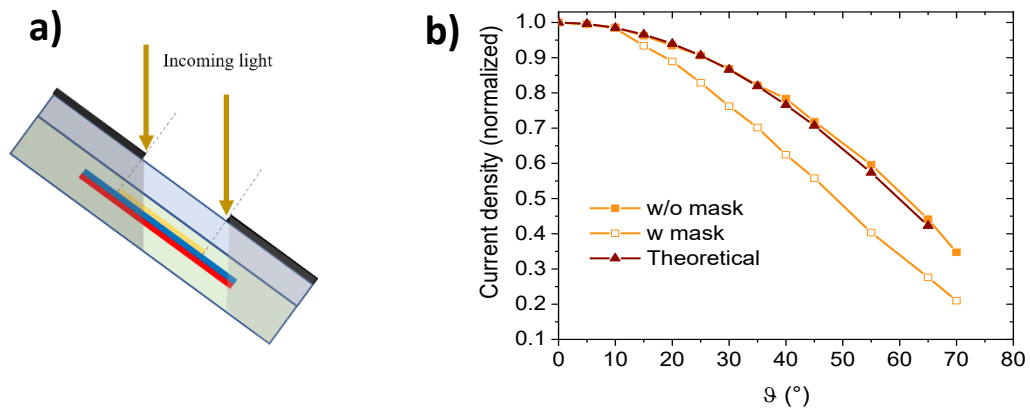
Figure 3.18: *a) Mask effect with increasing the angle. b) Comparison between the angular dependency Jsc for the devices with and without the mask and the theoretical behavior.*

experiments, we collected a JV curve of the tandem device for several theta, ranging from 0° to 70°. In our first experiments, we observed a discrepancy between the experimental values and the theoretical trend (Jsc (θ) = Jsc*cosθ). Indeed, the experimental Jsc was significantly lower at higher angles than what we expected. This variation arises from the presence of the shading mask, which we used to define the active area. Considering a standard measure, therefore with the incoming light perpendicular to the cell surface, without this shadow mask the current would be generated from the active area but also from the area where the top TCO is not deposited, leading to extra carriers' collection and thus overestimating the current. The portion of shaded area is shown in figure 3.17a. In a real module (figure 3.17b) the active area includes the whole device area, thus the shading mask would not be included in the final architecture. Indeed, because of the mask, increasing the AoI, a certain portion of the active area is shaded by the mask, and, in addition, the incoming light reaches the non active region (figure 3.18a). To avoid this artifact, firstly, we developed a correction factor based on geometrical considerations that allows us to evaluate the shaded area. However, our correction assumed a zero current generation in the shaded regions, which is not the case. Therefore, we were not able to
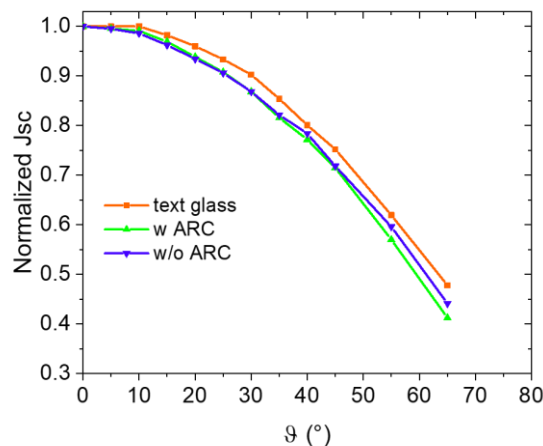

Figure 3.19: *Behavior of the normalized Jsc with the angle for the three different configurations.*

63

reproduce the theoretical behavior with a simple geometrical correction. Secondly, we repeated the experiments without the shadow mask, exploiting the carrier diffusion length of the silicon to compensate for the transport in the non active regions. Figure 3.18b shows the comparison between the angular dependency Jsc for the devices with and without the mask and the theoretical behavior. From the trends, we noted that the current density variation was mostly given by the presence of the mask while the experiment without was in well-agreement with the theoretical prediction.

Strengthened by this knowledge, we then shifted our focus on the exploration of potential technologies that can minimize the angular losses. As already discussed in the previous chapter, the presence of MgF_2 on top of the front glass or the adoption of a textured glass can mitigate the reflection losses and, therefore, increase the current output given by the module. Therefore, we encapsulated three tandems with different packaging: simple glass (reference), textured glass, and glass covered with MgF_2 ARC. Then, we collected the JV curves at different incident angles. The normalized Jsc plotted as a function of the angle for the different configurations is shown in figure 3.19. We noted that by increasing the AoI, the textured glass configuration shows the best response with higher values of Jsc compared to the other module architectures. On the contrary, the cell with the ARC on top of the glass does not show promising results.

Angular-dependent EQE

Since the current of monolithic tandems is always regulated by the current matching condition, to better understand the trends observed in the angular JV experiment we measured the EQE of each device at different angles (from 0° to 70°, angular-dependent EQE). We can use these measurements to evaluate the current of each sub-cell and relate it to the current output of the tandem in outdoor condition, to understand the limiting operating sub-cell at a given moment of the day. Moreover, the angular dependent EQE provides useful insights to evaluate the losses due to higher reflections. Figures 3.20 a, b and c show the EQE measurements at different angles for three modules with different front glasses: flat glass without ARC, flat glass with ARC, and textured glass. As the incident angle increases, the general EQE response decreases due to the enhancement of the reflection (in agreement to what we observed with the angular-JV). In addition, when the incident angle θ differs from zero, the path of the light through the layers (glass, encapsulant, perovskite, and silicon) increases, seen the materials thicker by a factor senθ, which leads to higher parasitic absorptions. Considering the flat front glass, the current delivered by the two subcells decreases proportionally conserving the current matching condition. To visualize the trend, we plotted the difference between the integrated EQE of the perovskite (which correspond to the current density generated by the perovskite sub-cell) and silicon (which correspond to the current density generated by the silicon sub-cell) as a function of theta (figure 3.20d). Until $\theta=50°$, the current matching condition is identical, with the perovskite generating more current than the silicon sub-cell. At higher angles, the perovskite and the silicon sub-cells generate almost the same current. For the module covered with the MgF$_2$ ARC the trend is different. In this case, at high angles ($\theta >$
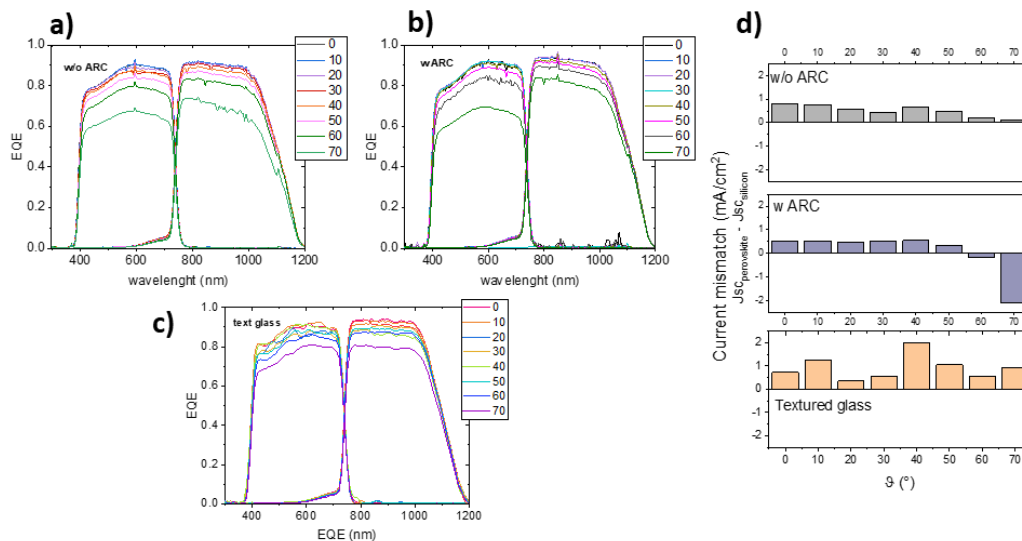

Figure 3.20: *Angular-dependent EQE signals a) without ARC, b) with ARC, c) with textured front glass. d) Current mismatches for the different module architectures.*
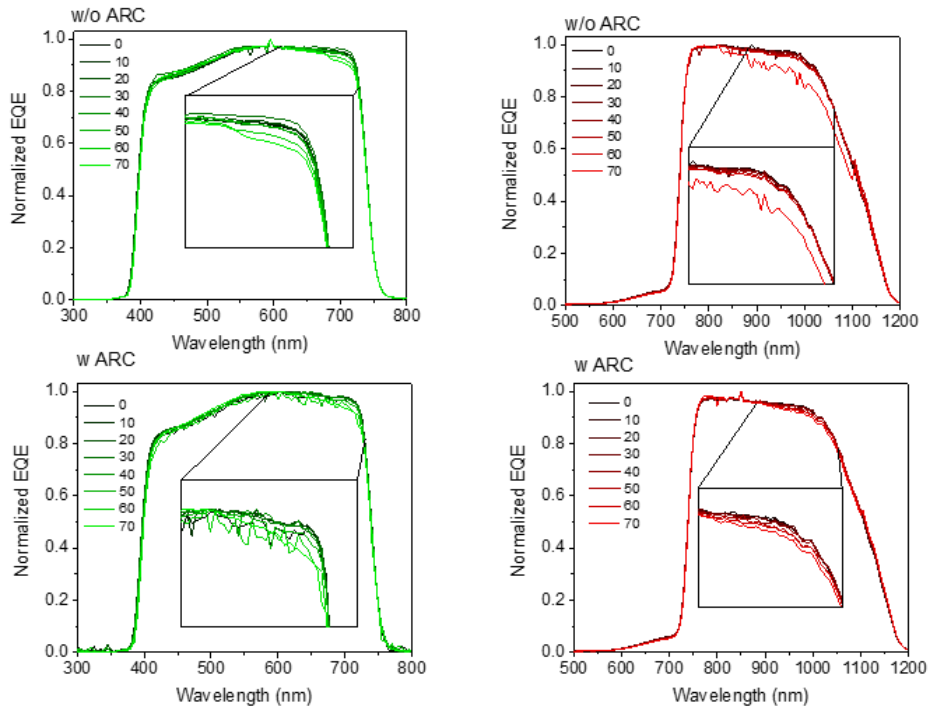
Figure 3.21*: Normalized EQE signals. On top, the perovskite and silicon normalized measurements for the reference minimodule (without ARC on glass), similarly below, the normalized EQE for perovskite and silicon subcells in the presence of ARC on top of glass.*

60°) the current matching condition inverts the trend, with the silicon sub-cell generating more current than the perovskite counterpart. This is due to the apparent thickness of the ARC layer that shifts the maximum of the reflection in the range of wavelengths absorbed by the perovskite sub-cell. The module with the textured glass does not show an inversion of the current matching condition, but we can observe a general higher value of the EQE signal for every value of angle, but in the other hand the glass texturing increases the current output from the perovskite sub cell leading to a significant mismatch for every value of angle. Since the textured glass leads to a higher angular mismatch compared with the other configurations, we opted to do not consider this configuration for a more in-depth investigation. Therefore, the signals, belonging to the reference minimodule and the one that presents the ARC on top of the glass, have been normalized (figure 3.21) and, for all of them, we can observe a loss in the high wavelength region that can be attributed to
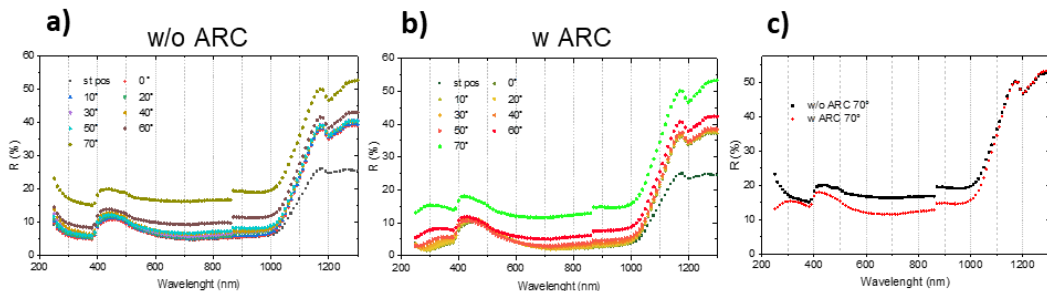

Figure 3.22*: Angular dependency reflection measurements for the two configurations. c) Comparison between the reflection measurements at 70°.*

66

reflection losses or a loss in the collection efficiency as the angle increases. To shed more light on the origin of this mechanism, we carried out angular dependency reflection measurements. In these measurements we faced a significant challenge due to the layout of the tandem. Indeed, in the EQE measurements, the spot size is relatively small, fitting well in the active area. However, for the reflection measurements, the sampling area is not limited to the tandem active area but includes also the non active regions (dead regions) and the silver electrode (whose nature significantly reflects the light). For this reason, we prepared two samples with the same layer stack used in the tandem cell, aside, for the top silver. We deposited the different layers over the entire bottom cell surface, and subsequently, we encapsulated the devices between two TPU sheets and two glasses (in one sample the top glass presented MgF_2 as ARC). To evaluate the angular dependency reflection a mount-center sample holder has been used (see chapter 2), placed inside the integrating sphere and different angles of incident (AoI) have been evaluated. The results, as expected, clearly show the reflection suppression given by the ARC for the region 250-1000nm, and the increase in the reflection signal with the angle (figure 3.22). However, when comparing the reflection with the EQE measure at 70°, we can observe that in the Si absorption region, in presence of MgF_2, the reflection signal is comparable to the reference one, which does not confirm what observed with the EQE measures. This can be explained because the only way to measure the reflection at different angles was to place the sample inside the integrating sphere. Because of this the total reflection collected by the detector
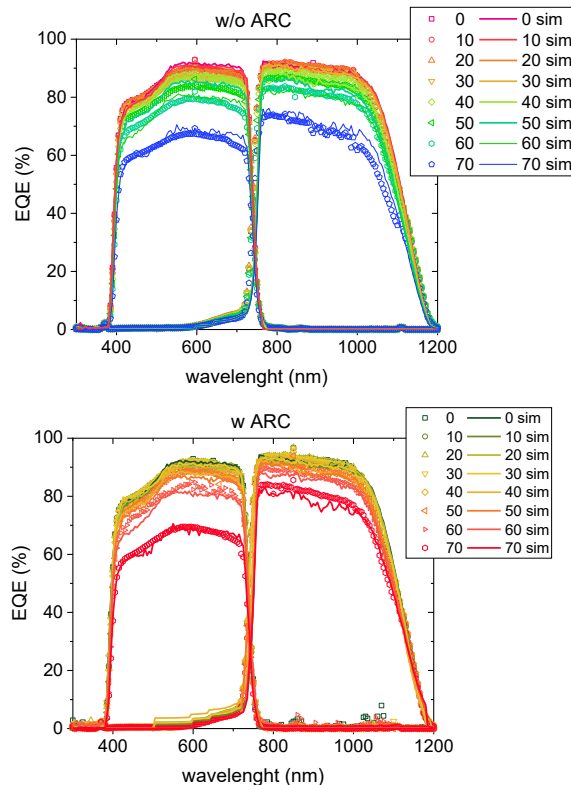

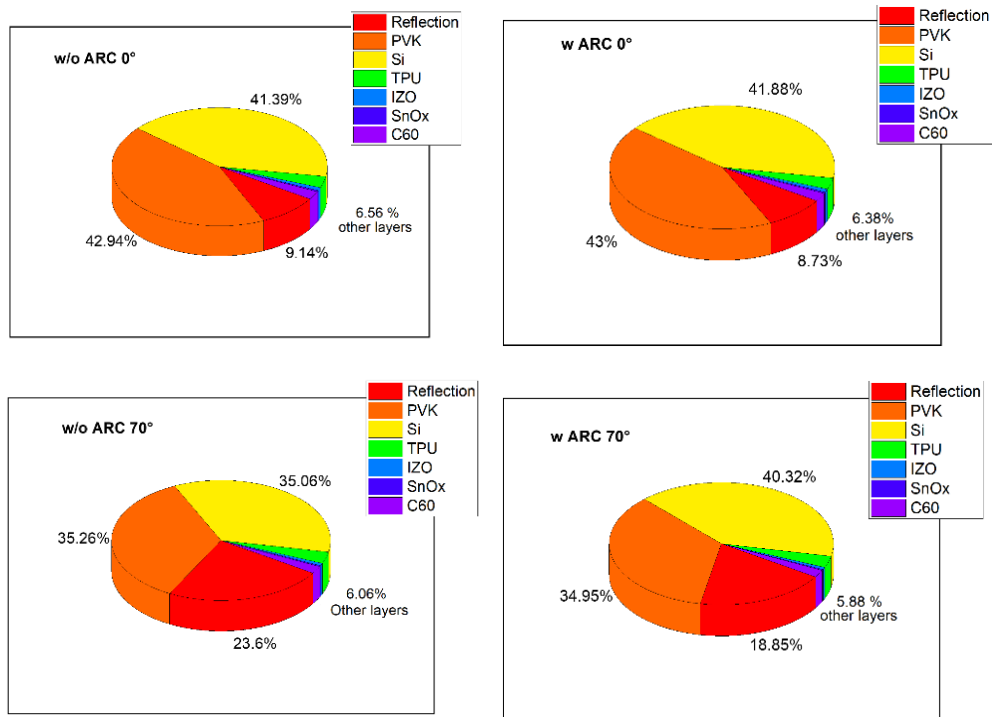*Figure 3.23: EQE simulated signals compared with the experimental data.*

Figure 3.24*: Portion of light absorbed by the different layers for 0° and 70°. The diagram also shows the total reflection.*

was given by the front and back surfaces of the sample leading to a higher reflection and the inability to disentangle the two contributes. Unable to rely on the reflection measures we seek support with optical simulation. Thanks to contribution of Dr Waseem Raja, we adopted a current simulation software to simulate the EQE data using the layout of our tandem, based on the refractive index (n) and the extinction coefficient (k) obtained from ellipsometry measurements. Figure 3.23 shows the comparison between the measured and simulated EQE data where we can observe that the simulation well matches with the experimental measurements. Therefore, to understand why in the presence of ARC on the glass the silicon subcell generates more current at high values of angle, thanks to the simulation we evaluated the different portion of light absorbed by the different layers as the angle increases (figure 3.24). At 70° in presence of ARC, the portion of light absorbed by the silicon subcell is greater than the silicon subcell at the same angle but without ARC. As already mentioned, the path light through the layers, increases as the angle increases. As a result, at 70° the MgF_2 thickness (considered as the distance that the light travels inside the MgF_2 layer) is now optimized to suppress the reflection for the silicon subcell and increase the portion of light absorbed by the bottom subcell. In a real-world condition, many other factors need to be considered. Depending on the Earth's location the real solar spectrum would be different from the AM 1.5G and also the intensity of the spectrum during the day. All these factors will lead to a different current match condition, therefore depending on the installation site, one configuration might be more suitable than another.

Outdoor results and lab comparison

To confirm our findings and prove their reliability to real applications of solar modules, we compared the angular dependency behavior of the current that we obtained in our experiments with the current generation of a tandem minimodule in outdoor conditions. The angular dependency laboratory set-up simulates only the elevation angle of the sun with a constant azimuth angle. For this reason, the minimodule was placed parallel to the ground. But, when the sun strikes the minimodule at the Kaust testing field location, the incident angle between a sun ray and the module surface cannot be described only with the elevation angle because the position of the sun during the day is also determined by the azimuth angle. Moreover, as already mentioned (section 2), in the testing field the minimodules were mounted with an angle of 25° south oriented because, this allows to maximize the power incident on the module surface over the course of the year (averaged between winter and summer insulation). Therefore, to evaluate the incident angle during the day we installed a simple set up resembling a sundial (schematically represented in figure 3.25a) where we evaluated the angle of incidence measuring the shadow generated by a rod-shaped object. Once evaluated the different values of angle, we compared the data (figure 3.25b). It is important to mention that the first value of the Jsc corresponds to an angle of incidence of around 17°. To understand the reason for this, we have to consider that these measures were collected on the 7th of May, when, at noon the elevation angle of the Sun was around 85° (as shown in the polar plot in figure 1.24) and, since the tilted angle of the module is 25°, the sun rays cannot be considered perpendicular to the module surface. As a result, the lowest value of angle between the module surface and the sun was around 17°. Moreover, during the day, the spectral power is not constant leading to lower values of the current density at high values of angles. However, we can clearly see that the
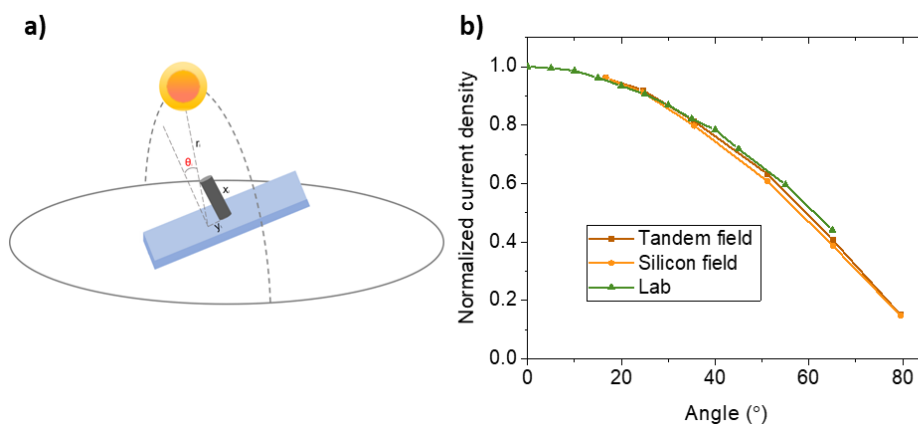
Figure 3.25: a) Schematic representation of the set-up adopted to evaluate the incident angle of the sun on the minimodule surface. b)Comparison between the data collected in the lab and in the outdoor testing field.

comparison between the 2 different angular dependent Jsc confirms the reliability of our set up. To further confirm our results, the Jsc behavior with angle for a silicon module was measured and compared with the experimental data.

Conclusion

Outlook and future studies

In this work, we demonstrated the possibility of manufacturing high performances perovskite/silicon tandem minimodule with a relatively long-term stability. We focused on the possibility of replacing EVA-based encapsulants with two new polymers, TPU and Borealis. These polymers are thermoplastic materials, enabling a reduction of the encapsulation temperature otherwise not possible with EVA, due to a certain threshold given by the crosslinking temperature. Moreover, these materials are less prone than EVA to delaminate the perovskite contact. Still, we realized that Borealis causes sporadic events of delamination. We found that the origin of this effect is sought in a higher Young modulus of Borealis compared to TPU. From an optical perspective, TPU is absorbing a remarkable part of the UV-blue spectrum of the sunlight, originating parasitic absorptions that limit the current of the perovskite subcell. On the contrary, Borealis is more transparent in the UV-visible region, maximizing the current output of the perovskite sub-cell; however, it has a weak absorption in the near-IR, concomitant with the absorption of the silicon sub-cells. This information is of paramount importance for designing efficient tandem modules. Indeed, to satisfy the current match condition, the choice of the encapsulant will dictate the perovskite bandgap (hence, its chemical formulation) and the optics of the silicon sub-cell. For example, if the silicon sub cell generates lower current than the perovskite top cell, we envision two strategies to preserve high power output. Firstly, improving the silicon bottom cell optics is less constrained than the perovskite (where the $IZO/SnO_x/C_{60}$ contact is practically the only available option). Indeed, the silicon response can be improved with rear reflectors, surface texturing, and by replacing amorphous silicon with nanocrystalline silicon oxide. These strategies will compensate for the decrease in the silicon response when Borealis is adopted in the module. Secondly, the perovskite band gap can be increased (switching to higher bromide content), leading to a higher voltage and lower current. In turns, this will match the current between the two subcells, but will capitalize the higher perovskite bandgap in a higher voltage output, boosting the power output. However, increasing the band gap and thus the Bromide content in the perovskite composition can affect the long term stability because of the halide segregation. For these reasons, TPU might be the initial encapsulant for the commercialization of perovskite/silicon modules. We also tested these materials in terms of stability, showing with preliminary tests that both encapsulants are reliable, withstanding 50 cycles of thermal cycling and 500h of damp heat, which are tests belonging to the IEC 61215 standards.

In the second part, we studied the angular-dependency current behavior of the perovskite/silicon tandem minimodules. We demonstrated that a thorough design of the module optics can improve the efficiency of the minimodule. This includes the adoption of ARC on the front glass or the adoption of textured glasses. These sophistications are particularly relevant, when the light is striking the surface perpendicularly ($\theta = 0°$) but might lead to a total lower power output during the day. Indeed, ARC on top of the glass leads to higher currents output at $\theta = 0°$ but as the angle increases the Jsc decreases more rapidly compared with the reference configuration (without ARC). Despite the ARC configuration, the textured glass shows the best Jsc angular dependency but on the other hand leads to a higher current mismatch throughout the day.

Overall, the important parameter that has to be taken into account is the levelized cost of electricity (LCOE) which is a measure of the average net cost of electricity generation for a generator over its lifetime. Therefore, improving the power output of the modules is equal to a cost reduction of the installation. Since the power output depends on the whole day generation, the adoption of ARC or textured glasses may have different impacts on the LCOE. For example, ARC may be more suitable for tracking installation, where the modules are perpendicular to the light for a longer portion of the day. On the contrary, textured glass may find applications in fixed-tilt installations, such as residential and rooftops.

So far, the enormous amount of effort that is being put in tandem solar cell research is mainly focused on the solar cell level and finding new materials that improve the efficiency. The knowledge at the device and the materials adopted have reached high levels, leading to high performance and stability improvements. But, in order to reduce the gap between the research level and the commercialization, studies regarding the transition from solar cells to PV modules and the validations of the modules under real world conditions are necessary to overcome the challenge. New encapsulant materials, looking at the perovskite constrain, can be developed and tested, such as low temperature crosslink materials or thermoplastic materials with high adhesion to the cell top electrode, without inducing delamination of the underneath layers. Moreover, looking at the outdoor performances, the real solar spectrum in a certain World's location differs from the AM1.5G spectrum. This leads to a different current mismatch condition. As a result, understanding the behavior of perovskite/silicon tandem solar cells at different World's location can help to understand which value of bandgap for the perovskite top cell is optimal or as an alternative the adoption of a different band gap depending on the location of the installation site.

Dissemination

List of publications

- "Monolithic Perovskite/Silicon Tandem Photovoltaics with Minimized Cell-to-Module Losses by Refractive-Index Engineering"

  Lujia Xu, Jiang Liu, Francesco Toniolo, Michele De Bastiani, Maxime Babics, Wenbo Yan, Fuzong Xu, Jingxuan Kang, Thomas Allen, Arsalan Razzaq, Erkan Aydin, Stefaan De Wolf

  ACS Energy Letter, **2022**, 7, 2370-2372.

- "Efficient and reliable encapsulation of perovskite/silicon modules"
  Francesco Toniolo, Michele De Bastiani, Maxime Babics, Jiang Liu, Erkan Aydin, Ahmed Ali, Lujia Xu, Thomas Allen, Moreno Meneghetti, Stefaan De Wolf

  Progress in photovoltaics, invited. *Manuscript under preparation.*

- "Angular-dependent performances of perovskite/silicon tandem in experimental and outdoor conditions"
  Francesco Toniolo, Michele De Bastiani, Waseem Raja, Maxime Babics, Thomas Allen, Moreno Meneghetti, Stefaan De Wolf

  Manuscript under preparation.

References

1. Li, L. *et al.* Review and outlook on the international renewable energy development. *Energy and Built Environment* **3**, 139–157 (2022).

2. Gerland, P. *et al.* World population stabilization unlikely this century. *Science (1979)* **346**, 234–237 (2014).

3. Lutz, W. & Kc, S. Dimensions of global population projections: what do we know about future population trends and structures? *Philosophical Transactions of the Royal Society B: Biological Sciences* **365**, 2779–2791 (2010).

4. Sinaga, R. *et al.* Photovoltaics module reliability for the terawatt age. *Progress in Energy* **4**, 022002 (2022).

5. World Energy Outlook 2020 – Analysis - IEA. https://www.iea.org/reports/world-energy-outlook-2020?mode=overview.

6. Ghosh, S. & Yadav, R. Future of photovoltaic technologies: A comprehensive review. *Sustainable Energy Technologies and Assessments* **47**, 101410 (2021).

7. Sapoval, B. & Charles, H. *Physics of semiconductors*. (Ellipses, 1988).

8. Peter Wurfel and Uli Wurfel. *Physics of Solar cells*. (Wiley-VCH, 2016).

9. Jenny Nelson. *The Physics of Solar Cells*. (Imperial college press).

10. Arno, S., Klaus, J., Olindo, I., Renè, V. S. & Miro, Z. *Solar energy, The physics and engineering of photovoltaic conversion, technologies and systems*. (UIT Cambrige Ltd, 2016).

11. Shockley, W. & Queisser, H. J. Detailed Balance Limit of Efficiency of p-n Junction Solar Cells. *Journal of Applied Physics* **32**, 510 (2004).

12. Best Research-Cell Efficiency Chart | Photovoltaic Research | NREL. https://www.nrel.gov/pv/cell-efficiency.html.

13. Ross, R. T. & Nozik, A. J. Efficiency of hot-carrier solar energy converters. *Journal of Applied Physics* **53**, 3813 (1998).

14. Tian, J. & Cao, G. Semiconductor quantum dot-sensitized solar cells. *http://dx.doi.org/10.3402/nano.v4i0.22578* **4**, 22578 (2013).

15. Rao, A. & Friend, R. H. Harnessing singlet exciton fission to break the Shockley–Queisser limit. *Nature Reviews Materials 2017 2:11* **2**, 1–12 (2017).

16. Tanabe, K. A Review of Ultrahigh Efficiency III-V Semiconductor Compound Solar Cells: Multijunction Tandem, Lower Dimensional, Photonic Up/Down Conversion and Plasmonic Nanometallic Structures. *Energies 2009, Vol. 2, Pages 504-530* **2**, 504–530 (2009).

17. Todorov, T., Gunawan, O. & Guha, S. A road towards 25% efficiency and beyond: perovskite tandem solar cells. *Molecular Systems Design & Engineering* **1**, 370–376 (2016).

18. Needleman, D. B. *et al.* Economically sustainable scaling of photovoltaics to meet climate targets. *Energy & Environmental Science* **9**, 2122–2129 (2016).

19. Allen, T. G., Bullock, J., Yang, X., Javey, A. & de Wolf, S. Passivating contacts for crystalline silicon solar cells. *Nature Energy 2019 4:11* **4**, 914–928 (2019).

20. Chakhmouradian, A. R. & Woodward, P. M. Celebrating 175 years of perovskite research: A tribute to Roger H. Mitchell. *Physics and Chemistry of Minerals* **41**, 387–391 (2014).

21. de Wolf, S. *et al.* Organometallic halide perovskites: Sharp optical absorption edge and its relation to photovoltaic performance. *Journal of Physical Chemistry Letters* **5**, 1035–1039 (2014).

22. Snaith, H. J., Petrozza, A., Ito, S., Miura, H. & Grätzel, M. Charge generation and photovoltaic operation of solid-state dye-sensitized solar cells incorporating a high extinction coefficient indolene-based sensitizer. *Wiley Online Library* **19**, 1810–1818 (2009).

23. Ball, J. M., Lee, M. M., Hey, A. & Snaith, H. J. Low-temperature processed meso-superstructured to thin-film perovskite solar cells. *Energy & Environmental Science* **6**, 1739–1743 (2013).

24. Liu, M., Johnston, M. B. & Snaith, H. J. Efficient planar heterojunction perovskite solar cells by vapour deposition. *Nature 2013 501:7467* **501**, 395–398 (2013).

25. de Wolf, S. *et al.* Organometallic halide perovskites: Sharp optical absorption edge and its relation to photovoltaic performance. *Journal of Physical Chemistry Letters* **5**, 1035–1039 (2014).

26. Stranks, S. D. *et al.* Electron-hole diffusion lengths exceeding 1 micrometer in an organometal trihalide perovskite absorber. *Science (1979)* **342**, 341–344 (2013).

27. Dong, Q. *et al.* Electron-hole diffusion lengths > 175 μm in solution-grown CH3NH3PbI3 single crystals. *Science (1979)* **347**, 967–970 (2015).

28. Kulkarni, S. A. *et al.* Band-gap tuning of lead halide perovskites using a sequential deposition process. *Journal of Materials Chemistry A* **2**, 9221–9225 (2014).

29. de Bastiani, M. *et al.* All Set for Efficient and Reliable Perovskite/Silicon Tandem Photovoltaic Modules? *Solar RRL* **6**, 2100493 (2022).

30. Jinko Solar-tiger Pro. https://www.jinkosolar.com/en/site/tigerpro#s1.

31. Game changer: Violet Power to offer 50-year solar panel warranty with US-made IBC technology – The Leading Solar Magazine In India. https://www.eqmagpro.com/game-changer-violet-power-to-offer-50-year-solar-panel-warranty-with-us-made-ibc-technology/.

32. Babics, M. *et al.* Unleashing the Full Power of Perovskite/Silicon Tandem Modules with Solar Trackers. *ACS Energy Letters* 1604–1610 (2022) doi:10.1021/ACSENERGYLETT.2C00442/ASSET/IMAGES/LARGE/NZ2C00442_0003.JPEG.

33. Liu, J. *et al.* 28.2%-efficient, outdoor-stable perovskite/silicon tandem solar cell. *Joule* **5**, 3169–3186 (2021).

34. US20210234101A1 - Hole-transporting self-organised monolayer for perovskite solar cells - Google Patents. https://patents.google.com/patent/US20210234101A1/en.

35. Fu, Z. *et al.* Encapsulation of Printable Mesoscopic Perovskite Solar Cells Enables High Temperature and Long-Term Outdoor Stability. *Advanced Functional Materials* **29**, 1809129 (2019).

36. Saliba, M. *et al.* Incorporation of rubidium cations into perovskite solar cells improves photovoltaic performance. *Science (1979)* **354**, 206–209 (2016).

37. Bush, K. A. *et al.* 23.6%-efficient monolithic perovskite/silicon tandem solar cells with improved stability. *Nature Energy 2017 2:4* **2**, 1–7 (2017).

38. Cheacharoen, R. *et al.* Encapsulating perovskite solar cells to withstand damp heat and thermal cycling. *Sustainable Energy & Fuels* **2**, 2398–2406 (2018).

39. Holzhey, P. & Saliba, M. A full overview of international standards assessing the long-term stability of perovskite solar cells. *Journal of Materials Chemistry A* **6**, 21794–21808 (2018).

40. Perovskite on silicon tandem solar cell technology | Oxford PV. https://www.oxfordpv.com/perovskite-silicon-tandem-cell.

41. Shi, L. *et al.* Accelerated Lifetime Testing of Organic-Inorganic Perovskite Solar Cells Encapsulated by Polyisobutylene. *ACS Applied Materials and Interfaces* **9**, 25073–25081 (2017).

42. de Bastiani, M. *et al.* Toward Stable Monolithic Perovskite/Silicon Tandem Photovoltaics: A Six-Month Outdoor Performance Study in a Hot and Humid Climate. *ACS Energy Letters* **6**, 2944–2951 (2021).

43. Azmi, R. *et al.* Damp heat-stable perovskite solar cells with tailored-dimensionality 2D/3D heterojunctions. *Science (1979)* **376**, 73–77 (2022).

44. de Bastiani, M. *et al.* Mechanical Reliability of Fullerene/Tin Oxide Interfaces in Monolithic Perovskite/Silicon Tandem Cells. *ACS Energy Letters* **7**, 827–833 (2022).

45. Ball, J. M. *et al.* Optical properties and limiting photocurrent of thin-film perovskite solar cells. *Energy & Environmental Science* **8**, 602–609 (2015).

46. Xu, L. *et al.* 26.2 %-efficient monolithic perovskite/silicon tandem modules with 18.6 mA/cm2 short circuit current density . *ACS energy letters Express* (2022).

Acknowledgments

Thanks to this experience I met a lot of people that left a sign in my journey, they helped me inside and outside the laboratory making the whole experience wonderful and without them, I would not be the person that now I am. I want to thank Prof. Moreno Meneghetti for his help and feedback during this thesis and Prof. Stefaan De Wolf for allowing me to have this amazing experience at KAUST accepting me into his group and making me understand what means to work in a research group.

In addition, I must thank two people, Dr. Michele de Bastiani who was the real mastermind behind this work, he imprinted in me as much passion and knowledge as possible, and Dr. Maxime Babics for always being available in helping me, discussing and solving the difficulties I encountered during this path. They were not only colleagues but friends, who allowed me to have experiences that I would not have been able to do without them, making this experience unforgettable. I am sure that without them I would not be here to write these words.

I am really grateful to all the people that helped me during this work like Dr. Thomas Allen for the help with the reflection measures, Dr. Jiang Liu for teaching me the manufacturing process of the cells, Dr. Waseem Raja, and Dr. Lujia Xu for the data simulation. I wish all the best to all the KPV lab group, and I really want to thank everyone from the deep of my heart.

Non posso concludere senza aver ringraziato le persone che mi sono state vicine durante questo percorso, mi hanno spinto a dare il meglio e mi hanno sempre supportato, in particolare tutti gli amici e Chiara, la quale è sempre stata il mio porto sicuro, supportandomi non facendomi mai mollare, grazie a lei e alla forza di volontà che mi ha sempre trasmesso sono riuscito a raggiungere il traguardo.

Ultimi ma non meno importanti vorrei ringraziare i miei genitori, i quali mi sono sempre stati accanto, non hanno mai creato impedimenti lasciandomi scegliere il mio percorso e supportandomi.

Grazie.